DEGRADATION MECHANICS OF BONE AND BONE LIKE MATERIALS VIA MULTISCALE ANALYSIS

by

MD FARZAD SARKER

Presented to the Faculty of the Graduate School of

The University of Texas at Arlington in Partial Fulfillment

of the Requirements

for the Degree of

DOCTOR OF PHILOSOPHY

THE UNIVERSITY OF TEXAS AT ARLINGTON

August 2014

Acknowledgements

Though only my name appears on the cover of this dissertation, a great many people have contributed to its production. I owe my gratitude to all those people who have made this dissertation possible and because of whom my graduate experience has been one that I will cherish forever.

My deepest gratitude is to my advisor, Dr. Ashfaq Adnan. I have been amazingly fortunate to have an advisor who gave me the freedom to explore on my own, and at the same time the guidance to recover when my steps faltered. His patience and support helped me overcome many crisis situations and finish this dissertation. He always kept me motivated through his wisdom, knowledge and commitment to work.

I would like to thank the members of my doctoral committee, Dr. Harry F. Tibbals, Dr. Wen S. Chan, Dr. Kent L. Lawrence and Dr. Majid Minary for their input, valuable discussions and accessibility. I would like to thank the department of Mechanical and Aerospace Engineering at UTA, especially Dr. Seiichi Nomura for being a wonderful graduate advisor.

I am also grateful to the following staff at The University of Texas at Arlington, for their various forms of support during my graduate study—Debi Barton, Lanie Gordon, Janet Gober, Louella Carpenter, Sally Thompson and Catherine Gruebbel.

Most importantly, none of this would have been possible without the love and patience of my parents, sisters and wife. My parents to whom this dissertation is dedicated to, have been a constant source of love, concern, support and strength all these years living eight thousand miles away from me. I would like to express my heart-felt gratitude to my parents for their faith in me and allowing me to be as ambitious as I wanted. I would like to thank my wife Shoshi. Her support, encouragement, quiet patience were undeniably helpful over the past years.

Above all, I am indebted to Allah Almighty for endowing me with health, patience and knowledge to complete this work.

July 11, 2014

Abstract

DEGRADATION MECHANICS OF BONE

AND BONE LIKE MATERIALS VIA

MULTISCALE ANALYSIS

Md Farzad Sarker, PhD

The University of Texas at Arlington, 2014

Supervising Professor: Ashfaq Adnan

Bone fracture is a common health risk for older people suffering from bone disease like osteoporosis. The more severe the osteoporosis is the more structural degradation in bones occurs, which eventually makes bones more fracture prone. The mechanical behavior of bone depends on the structural response of bone constituents over a broad range of length scales spanning from the nanoscale collagen fibril level to the macroscale trabeculae level. As such, in order to understand bone fracture, it is important to know the structure-property relations of bone material over the entire length of scale. Surprisingly, a quantitative understanding of bone fracture toughness is still not well understood, which the premise of the current study is. The multiscale analysis of bone is performed by considering five distinctive microstructures of bone, namely, the nano scale, submicron scale, micron scale, macro scale and trabecular bone itself. These substructures span almost over 9 order of length scales. By considering the nanoscale collagen fibril, the building block of bone composed of collagen protein (TC) and hydroxyapatite (HAP) mineral crystal, as a discontinuous fiber reinforced composite structure, the Halpin-Tsai relation for discontinuous fiber reinforced composites were used as the initial process for calculating mechanical properties of HAP and TC in nano scale. From the hierarchical level 2 to level 5, a self-similar approach was used to determine the mechanical properties of subsequent microstructures. Then, these properties were applied on

several finite element models consisting of several fully three dimensional solid trabecular model (obtained from direct micro CT scan) and five different "approximated spongy" microstructures with appropriate boundary conditions. Each approximated model represents a simplified microstructure of the trabecular network. Critical stress intensity factor or fracture toughness was calculated from linear elastic fracture mechanics theories using the constitutive model developed from multi-scale analysis. The effects of trabecular thickness on Mode I fracture toughness were studied with different models of different thickness and their relations were analyzed. A comparative study of structural stiffness and anisotropy was conducted between the CT scan image based real bone microstructure and approximated simplified bone like microstructures. Finally, a 3D printing based manufacturing method was adopted to fabricate and characterize SiC nanoparticle reinforced nanocomposites using the micro CT image we studied. The stress-strain response was measured and deformation mechanism was studied.

Table of Contents

List of Illustrations

List of Tables

Chapter 1

Introduction

Bone is a hard tissue made of two characteristic components at the macroscopic level – the cortical (compact) bone that forms a hard outer layer, and the cancellous (trabecular) bone that fills the interior spaces and ends of long bones (Rho et al., 1998). The cancellous bone has a foam-type microstructure that is built from three dimensional assembly of trabeculae (Evans et al., 1973). Individual trabecula has a multiscale microstructure spanning from the nanoscale to the microscale. Based on the high resolution micrographs and image analysis, it is possible to identify four distinct substructures that form the final structure of individual trabecula. These substructures, shown sequentially from the smaller scale to the larger scale in Fig. 1-1, are the (Rho et al., 1998) collagen and hydroxyapatite, (Evans et al., 1973) single collagen fibril, (Hamed et al., 2012) single collagen fiber, and (Fratzl et al., 1997) collagen fiber array bundles (Hamed et al., 2012; Fratzl et al., 1997). The four different length scales shown in Fig. 1-1 are termed as level one to level four.

A highly ordered assembly of collagen matrix and crystalline hydroxyapatite (Fratzl et al., 1997) forms the base of a single collagen fibril. In a collagen fibril, the longitudinal collagen matrix elements are 300 nm in length and staggered from each other by about 67 nm (Jager et al., 2000). The hydroxyapatite crystals are 50 nm in length, 25nm in width and 3nm in length and placed inside the collagen matrix with a defined length gap of 27nm. When assembled, the cylindrical nanocomposite structure is called collagen fibril with an average diameter of 50-200 nm and length several micrometers (Fratzl et al., 1997; Jager et al., 2000).

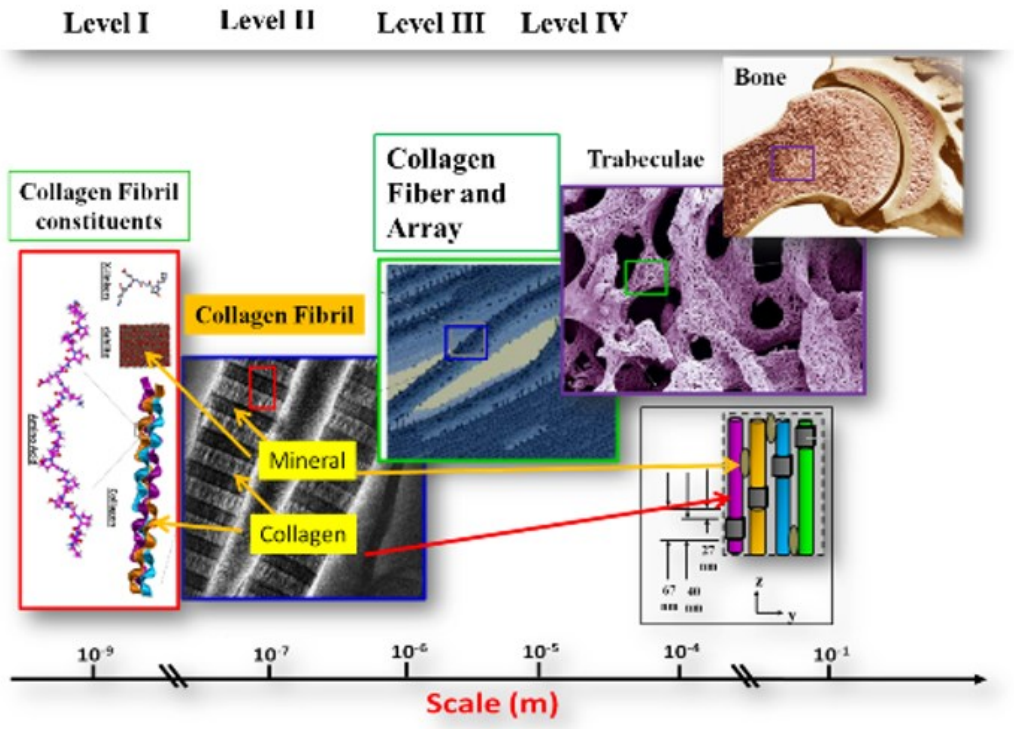

Figure 1-1 Hierarchical Structure of Bone

When collagen fibrils are bundled together to form a larger cylinder, the bundle is called collagen fiber with average diameter of 3-7μm. While individual collagen fibrils are semi-crystalline, the collagen fibers are almost crystalline (Fratzl et al., 1997; Jager et al., 2000). The next substructure is called collagen fiber array which is a bundle of collagen fibers. Each of these bundles is called single trabeculae or ligament for the trabecular system. A bundle of collagen fiber or collagen fiber arrays has a diameter of 50μm. These bundles are also crystalline (Fratzl et al., 1997).

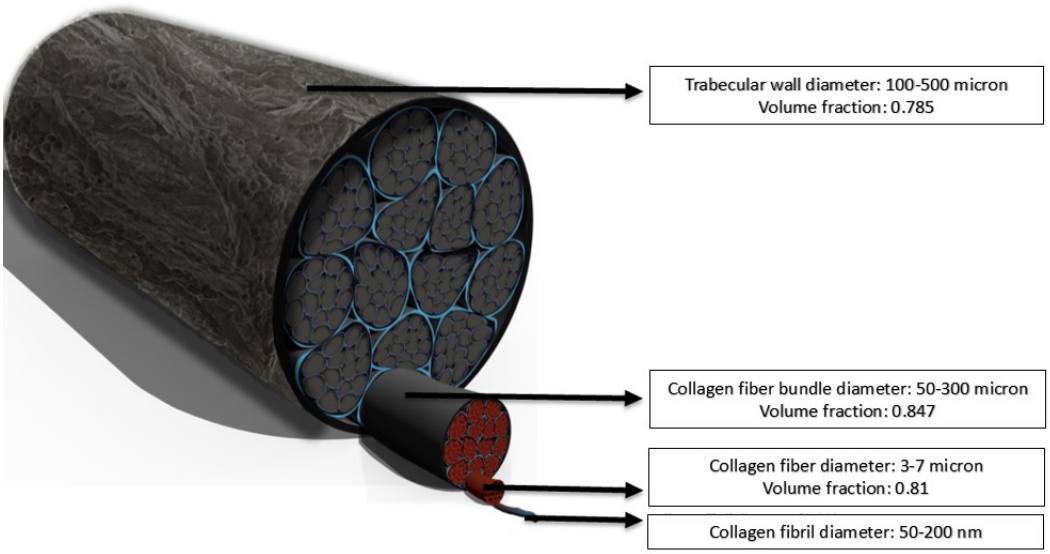

Figure 1-2 Collagen fiber bundle structure

Trabeculae microstructure is formed by three dimensional networks of collagen fiber arrays. It is the spongy part of bone and bone marrow is protected by it. The trabecular wall is a rod-like structure which is the macroscopic building block components of cancellous bone. The micro structure of trabecular bone is built upon random distributions of trabecular units. This part of bone is not as strong as compact bone. Therefore, fracture in bone most likely starts from the spongy part of bone. As such, predicting fracture toughness from this part is very important. Measuring fracture toughness or critical stress intensity factor of this segment of bone are one of the key aspects in this study.

As mentioned, the building block of trabeculae at the nanoscale is known as collagen fibril which is essentially a nanocomposite material made of soft collagenous matrix (TC) and hard hydroxyapatite (HAP) based hard minerals (Porter et al., 2004). It can be argued that the mechanical performance of bone at the macroscopic level largely depends on the mechanical response of this nanoscale building block and the translated properties to the upscale substructures. In other words, the prediction of the mechanical properties of the HAP-TC nanocomposites and understanding of

the translated properties at the upper scales is essential for quantitatively analyzing the fracture mechanisms of "cellular" trabecular bone.

Obtaining fracture toughness of cellular solids was studied by many groups. Gibson and Ashby studied the structure and mechanical behavior of cellular solids, engineering designs and fabrications (Gibson et al., 1999). Determining mode I fracture toughness of foam like materials was studied by a large number of groups. Choi and Shanker developed a finite element based micromechanical method for predicting mode I, mode II and mixed mode fracture toughness of cellular solids (Choi et al., 2003). In another study carbon foam was analyzed to predict mode I fracture toughness. K. Y. G. McCullough, N. A. Fleck and M. F. Ashby studied the fracture behavior of closed cell aluminum based foam and tested the toughness (McCullough et al., 1999). R. B. Cook & P. Zioupos studied an experimental determination of fracture toughness of femur (Cook et al., 2010). Norman TL, Vashishth D, Burr DB studied the longitudinal fracture toughness of human cortical bone under tension which is much stronger than cancellous bone on the longitudinal and transverse cross-sectional surfaces (Norman et al., 1995). Iwona studied toughness of bone based on Elastic properties and hardness of individual lamellae in bone's microstructure (Hamed et al., 2012).

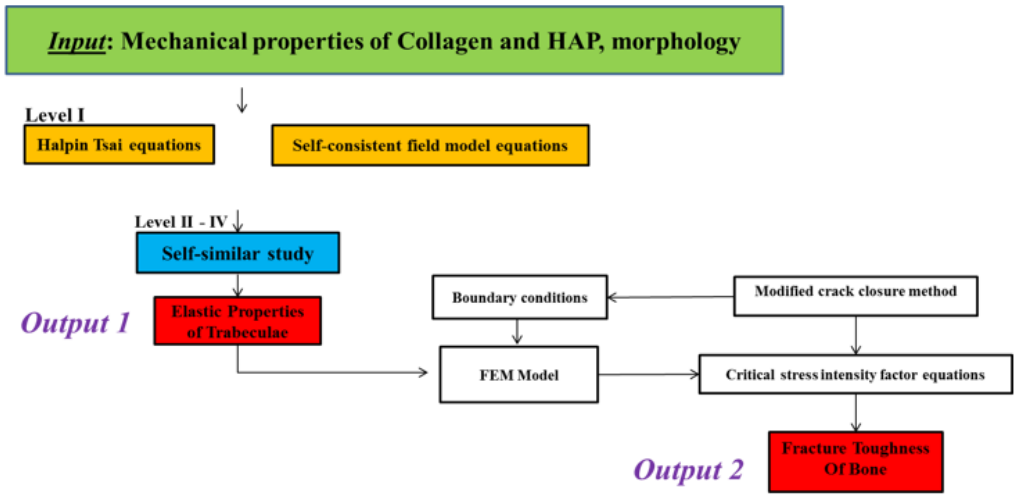

Figure 1-3 Flowchart showing essential steps involved in predicting stiffness and fracture toughness of trabecular bone

Our analysis was started with the predictions of the mechanical properties of collagen fibril. These properties were used to calculate all the next level mechanical properties of the hierarchical bone structure. Using transversely isotropic elastic properties for collagen and apatite, orthotropic properties of the upper-scale sub-structures were extracted and used in the finite element analysis (FEM) of trabecular bone. A study of fracture toughness (Adnan et al., 2010) of real trabecular bone and approximated bonelike cellular solid was done using the multiscale elastic properties of bone. In this study three different types of micro CT scan images were used:

- A 61 year old male human femoral neck.
- Artificially stimulated osteoporotic femur of young laboratory rats (C57/B6).
- 6 months old pig (Sus scrofadomestica) femoral head, raised under diets satisfying appropriate nutrient levels.

The approximated microstructures were three dimensional compact possible packing of

- Triangular prism

- Rectangular prism
- Hexagonal prism
- Rhombic dodecahedron
- Truncated octahedron.

These models were used to estimate the comparison of fracture toughness, structural stiffness and anisotropy behavior. The elastic properties of individual trabeculae ligaments were estimated by bottom-up analysis from nano scale constituents of real bone. The following Sections outline the methods and models with detailed discussions. The simulated results, process and comparisons are summarized in the following sections.

Chapter 2

Overview/Framework of the Methods and Models

Collagen is one of the most essential structural proteins found abundantly in all living animals. In human bodies, collagens are found in fibrous tissues such as tendon, ligament, cartilage, bone etc. and comprise 25% to 35% of the total body proteins. In bone, collagens combine with mineral cements to form composite fibril structure. These mineralized collagens are considered as the fundamental building block of bone. These building blocks form a hierarchical structure that controls the overall properties of bone including strength, stiffness and toughness. At the macroscopic level, bone tissue can be either cancellous (spongy) or cortical (compact) type. Since compact bones are significantly denser than cancellous bones, their mechanical properties are also significantly higher than cancellous bone. As a result, it is the cancellous bones that experience fracture during skeletal loading. As shown in Fig. 1-1, there are several distinct building blocks exist in the hierarchical organization in bone, which are outlined here in the context of trabecular bone. The spongy bone is composed of trabecular network that is formed when several 'rod' or 'plate' shaped trabeculae meet at the trabecular node. Individual trabecula is composed of lamellar array of composite fibers. Each fiber is the result of self-assembled collagen fibrils, where each fibril is formed by a staggered arrangement of mineralized tropocollagen molecules. Mineralization of collagen is achieved by deposition of dahllite crystals in the 'hole' region of collagen stacks. The fundamental constituents of collagen fibril are type 1 collagen, dahllite nanocrystals and non-collagenic cross linkers. Each collagen molecule in the fibril is formed from three chains of amino acids.

Morphologically, trabecular bone is a highly porous (60-95%) cellular material in which lamellar packets form together in a latticework of rod- and plate-like structures. The rod and plate structures (trabeculae) are typically 100-300 □m thick in human bone, and are separated by larger

marrow spaces with characteristic dimensions of 500-1000 □m. Structurally, the basic building block of cancellous bone is a composite material consisting of a hydrated (25% water) organic matrix (25%) stiffened by extremely dense calcium phosphate crystals (50%). The matrix contains 90% collagen type I and 10% other protein such as glycoprotein, osteocalcin, osteonectin etc. This composite block is called mineralized collagen fibril.

As such, it can be argued that the mechanical properties of bone at the macroscopic level are directly dependent on the mechanical properties of mineralized collagens. Therefore, it is very important to know how molecular-level mechanical properties of collagen fibrils are translated to the tissue level. It is also essential to know about the key factors that control the mechanical response of bone from its building block (collagen fibril) level. A quantitative knowledge of collagen mechanics will not only help the scientific community to understand overall bone mechanics but also provide a systematic guideline for advancing medical diagnosis/treatment protocol and tissue engineering.

The collagen in human is mostly Type 1 collagen, called tropocollagen (TC), consisting of helically arranged three polypeptide chains. The mineral in the bone is called dahllite which is 95% pure carbonated hydroxyapatite (HAP - $Ca_{10}(PO_4)_6(OH)_2$). Type I collagen is formed in bone from the combination of collagen polypeptides containing specific sequence of amino acids (residues). This structure is known as procollagen. One end of the procollagen contains amine group (NH_3) and the other end contains carboxyl group (COOH). Because of this collagen ends are regarded as N-terminal and C-terminals. As shown in Fig.1-2, the mineralized collagen fibrils are formed by staggered self-assembly of ~300 nm long collagen molecules and dahllite nano-block (50nm×25nm×3nm). All 300 nm long collagen molecules (zx plane) self-assemble into fibrils with a specific tertiary structure having a 67 nm periodicity and 40 nm gaps or holes between the ends of the molecules. Each collagen molecule is linked to each other by three distinct cross-linking agents (NTx, CTx and ICTP) located at the N-terminal, C-Terminal and intermediate position.

2.1 Overview of the Methods

2.1.1 Macro Scale Bone Properties: Bottom up Elastic Property Calculation from Collagen Fibril:

Trabecular bone has a porous structure with a lot of struts. These single struts' properties were obtained from the smallest constituents of bone. The separate properties of collagen and hydroxyapatite were extracted from molecular dynamics simulations. A mathematical model was developed to do the bottom up calculation of elastic properties.

In our study, five different scales were explored and among these five scales, properties of four scales were calculated. These five scales are collagen fibril, collagen fiber, collagen fiber array bundles, trabecular wall (ligament) and trabecular network (Hamed et al., 2012; Jager et al., 2000). Since the fifth scale represents the trabecular network itself, its properties can be estimated from the network morphology and the trabecular wall properties. In other words, the first four scales define the overall material properties of bone and the fifth scale defines the structural properties of bone. In this study, the first four scales were named as level one (the smallest scale) to level four (largest scale) accordingly.

The structure of the first scale is built upon two basic units, collagen and hydroxyapatite. In the context of composite material, the collagen and hydroxyapatite is combined together like matrix and fiber to form "nanocomposite" collagen fiber. Structurally, the collagen matrix is weaker than hydroxyapatite fiber. In the upper scales, namely at the sub micro and micro scales, the "fibrillar collagen" bundles and other "soft" proteins together create a composite like environment. Here, the collagen fibril bundles behave like fiber and the "softer materials" behave like matrix. Together they form composite sub-structure in every scale (Hamed et al., 2012; Fratzl et al., 1997; Jager et al., 2000; Adnan et al., 2010). In this study, the theories of composite materials (Hull et al., 1996) are

used to analyze the mechanical properties of every single scales of bone. The flowchart shown in Fig. 1-3 outlines the essential steps involved.

Table 2-1 Elastic properties of Collagen and Hydroxyapatite

E_f	E_m	G_f	G_m	V_f	V_m	ν_f	ν_m
120 GPa	0.5GPa	45GPa	0.2GPa	0.7	0.3	0.27	0.3

The calculation starts from the individual properties of collagen and hydroxyapatite. Based on the morphology of collagen and hydroxyapatite crystals, we have assumed that both materials possess transversely isotropic material symmetry. Table 1 shows the mechanical properties of hydroxyapatite and collagens, and Table 2 shows dimensions of hydroxyapatite crystals that are used in this study.

Table 2-2 Dimensions of Hydroxyapatite

Length (L)	Width (W)	Height (H)
50 nm	25 nm	3 nm

We argue that when these two transversely isotropic constituents are combined to form the collagen fibril, the composite material will have orthotropic material symmetry, which requires nine independent elastic constants. These are: E_{11}, E_{22}, E_{33}, G_{12}, G_{23}, G_{13}, v_{12}, v_{13} and v_{23}. We have utilized the classical Halpin-Tsai (Halpin et al., 1976), rule-of-mixture and self-consistent methods (Isaac et al., 1994) to determine these nine constants.

It is known that Halpin-Tsai model is a mathematical model for the prediction of elastic constants of composite material based on the geometry and orientation of the filler and the elastic properties of the filler and matrix (Halpin et al., 1976; Isaac et al., 1994). The Halpin-Tsai models are used to describe 2-phase composites in which the matrix phase is isotropic. Halpin-Tsai materials may be transversely isotropic, orthotropic, or isotropic, depending on the geometry of the material reinforcing the matrix. In principle, there are five different Halpin-Tsai material models available: the continuous fiber model, the discontinuous fiber model, the continuous ribbon model, the discontinuous ribbon model, and the particulate model (Isaac et al., 1994). In this study, we used the "discontinuous fiber" model to determine the "in-plane" properties of the collagen fibril, namely, E_{11}, E_{22}, and G_{12}. The "in-plane" Poisson's ratio v_{12} was determined via rule-of-mixture. The following equations are used (Isaac et al., 1994).

$$E_{11} = \frac{1+2\left(\frac{l_f}{d_f}\right)\eta_L V_f}{1-\eta_L V_f} E_m \tag{1}$$

$$E_{22} = \frac{1+2\eta_T V_f}{1-\eta_T V_f} E_m \tag{2}$$

$$G_{12} = G_{21} = \frac{1+\eta_G V_f}{1-\eta_G V_f} G_m \tag{3}$$

$$\nu_{12} = \nu_f V_f + \nu_m V_m \tag{4}$$

$$\eta_L = \frac{\left(\frac{E_f}{E_m}\right)-1}{\left(\frac{E_f}{E_m}\right)+2\left(\frac{l_f}{d_f}\right)} \tag{5}$$

$$\eta_T = \frac{\left(\frac{E_f}{E_m}\right)-1}{\left(\frac{E_f}{E_m}\right)+2} \tag{6}$$

$$\eta_G = \frac{\left(\frac{G_f}{G_m}\right)-1}{\left(\frac{G_f}{G_m}\right)+2} \tag{7}$$

To obtain other constants, a set of equations were used from different sources (Cooper et al., 2007). The self-consistent field model yields an expression for the transverse composite modulus in terms of bulk and transverse shear moduli (Isaac et al., 1994). Bulk and transverse shear moduli

can be obtained using the equations (8) through (12). These two equations were used to obtain the shear moduli and Poisson's ratio of the plane perpendicular to the plane of isotropy. In this study, direction 1 was the longitudinal direction and the other two directions are considered equivalent and transverse directions. The following equations were used to determine G_{23} and v_{23}. Since the direction 2 and 3 are equivalent, it is conceivable that $E_{22} = E_{33}$, $G_{13} = G_{12}$, and $v_{12} = v_{13}$. By this, all constants are approximated for the collagen fibril or for "Level I".

$$G_{23} = \frac{G_m\left(\left(K_m\left(G_m+G_{23_f}\right)\right)+\left(2G_{23_f}G_m\right)+\left(K_m\left(G_{23_f}-G_m\right)V_f\right)\right)}{\left(K_m\left(G_m+G_{23_f}\right)\right)+\left(2G_{23_f}G_m\right)-\left(K_m+2G_m\right)\left(G_{23_f}-G_m\right)V_f} \tag{8}$$

$$K_2 = \frac{(K_f+G_m)K_m+(K_f-K_m)G_mV_f}{(K_f+G_m)-((K_f-K_m)V_f} \tag{9}$$

$$K_f = \frac{C_{11_f}+C_{12_f}}{4} \tag{10}$$

$$v_{23} = 1 - \frac{E_2}{2K_2} - 2\frac{v_{12}^2E_2}{E_1} \tag{11}$$

$$K_m = \frac{C_{11_m}+C_{12_m}}{4} \tag{12}$$

As shown in Fig. 1-2, each collagen fiber (Level II) is formed by bundling many collagen fibrils and each collagen fiber array (Level III) are formed by bundling many collagen fibers. When collagen fiber arrays are bundled together, then a single rod or plate of trabeculae is formed (Level IV), which is essentially the basis of cellular network of the trabecular system. Since the arrangement of level II thru IV are structurally very similar, we used a combination of Halpin-Tsai equation, self-similar approach and rule of mixture (Isaac et al., 1994) method to determine the elastic constants for these three levels.

We assume that a collagen fiber is cylindrical in shape because it is formed by packing bundles of cylindrical shaped collagen fibrils. We further assume that the cross-sectional area of a single collagen fiber includes densely packed circles that represents individual collagen fibril, and excluded spaces, primarily occupied by softer non-collagenic materials (Hamed et al., 2012; Jager

et al., 2000). Hypothetical cross-sections of collagen fiber (Level II), fiber array (Level III) and trabecular rod (Level IV) is shown in Fig. 1-3 to demonstrate the "self-similar" morphology of different hierarchical levels of bone. It is obvious that if properties of the materials within the inner circles and the excluded spaces are known, then overall properties of that level can be estimated using rule-of-mixture analysis. Such analysis, of course, is vastly dependent on the volume fraction of the excluded space. We estimated the volume fraction of fibrillar materials at each level by using circle packing theory (Specht, E.). Our result is consistent with the findings of Iwona and Hamed. All essential equations to determine the elastic constants are provided in equations 13 thru 16.

$$E_{11_j} = E_{11_i} V_{f_j} + E_{w_j} V_{w_j} \quad (13)$$
$$E_{22_j} = E_{22_i} V_{f_j} \quad (14)$$
$$G_{12_j} = G_{12_i} V_{f_j} \quad (15)$$
$$\nu_{12_j} = \nu_{12_i} V_{f_j} + \nu_{m_j} V_{m_j} \quad (16)$$

Based on the self-similar analysis, the elastic properties for the Level-4 structure are obtained. From the elastic properties the tensors for level four were obtained which was used throughout the study for all finite element simulations.

Table 2-3 Elastic constants of bone at different hierarchical levels

Levels	E_1 (Gpa)	E_2 (Gpa)	E_3 (Gpa)	G_{12} (Gpa)	G_{23} (Gpa)	G_{13} (Gpa)	ν_{12}	ν_{23}	ν_{13}
L-1	11.8	3.86	3.86	1.09	0.574	1.09	0.279	0.42	0.279
L-2	9.58	3.12	3.12	0.885	0.464	0.885	0.225	0.34	0.225
L-3	8.11	2.64	2.64	0.75	0.394	0.75	0.191	0.29	0.191
L-4	6.37	2.07	2.07	0.589	0.309	0.589	0.15	0.22	0.15

The corresponding 3D elastic compliance matrix obtained from the elastic properties of level four or of trabecular bone is shown below:

$$\begin{bmatrix} 1.56 & -0.0235 & -0.0235 & 0 & 0 & 0 \\ 0 & 4.83 & -2.028 & 0 & 0 & 0 \\ 0 & 0 & 1.569 & 0 & 0 & 0 \\ 0 & 0 & 0 & 17.42 & 0 & 0 \\ 0 & 0 & 0 & 0 & 200 & 0 \\ 0 & 0 & 0 & 0 & 0 & 200 \end{bmatrix} 10^{-10} \quad (\text{MPa}^{-1})$$

These properties were used to predict fracture toughness of the "ideal" trabecular bone.

2.1.2 Developing a Mathematical Model to Predict Fracture Toughness of Porous Structures:

In this section, we describe a finite element based-fracture mechanics model to estimate the fracture toughness of the cellular trabeculae as a function of apparent density. Only Mode I fracture is considered in the present study. The basic steps followed to determine the fracture toughness of trabecular bone is outlined in the flowchart shown in Fig. 1-3. It is apparent that the properties of trabecular rods (Level IV) are the main input properties in the FEM analysis of bone. At first, a two dimensional beam model was used for FEM which was an estimated representation of the trabecular network. The morphology of the model was varied by changing the cross-sectional area of its cell ligaments', which essentially changes the apparent density of the model. The weight per unit volume of a material including is defined as apparent density.

The critical stress intensity factor of the cellular trabecular system was determined using the following equation [Choi and Shankar]:

$$\frac{K_I}{K_{IC}} = \frac{\sigma_{max}}{\sigma_{ulimate}^{solid}} \tag{17}$$

Here, K_I is the Mode I stress intensity factor of the cellular solid due to a prescribed tensile displacement, σ_{max} is the corresponding maximum developed stress along the loading direction, K_{IC} is the desired critical stress intensity factor and $\sigma_{ulimate}^{solid}$ is the ultimate strength of solid trabeculae (Level IV).

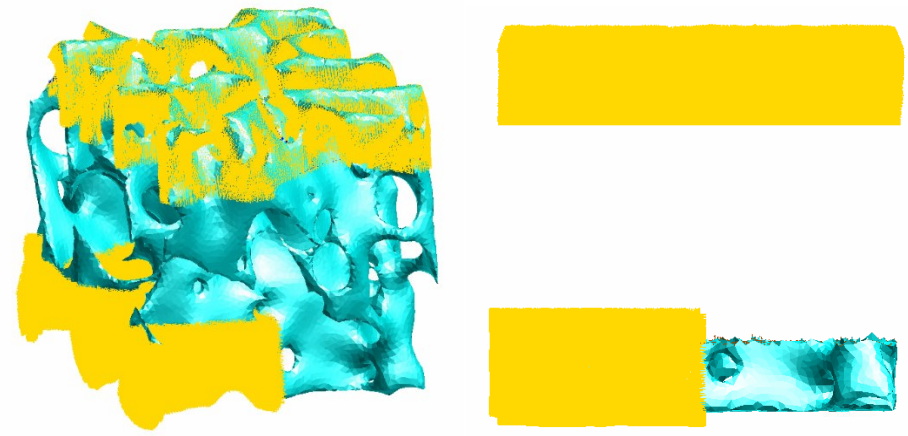

Figure 2-1 Loading of the trabecular bone for fracture toughness study

An arbitrary vertically upward displacement was applied on the quarter models shown in Fig. 2-1. It also shows the location of "maximum developed stress" in the second figure where the yellow band ends. The top yellow is applied tensile displacement and the bottom yellow is the fixed part. The modified crack closure method (Adnan et al., 2010) is used to calculate the mode I energy release rate G_I from the FEA result using the following relations:

$$G_I = \frac{1}{\Delta a} F_{tip}^{max}[u] \tag{18}$$

Where F corresponds to the vertical component of nodal force at node distanced Δa from crack tip, u corresponds to the vertical component of displacements at node distanced Δa from crack tip. Once, G_I is determined, the corresponding K_I is estimated using the method described by (Sih et al., 1965). It is known that cubic crystals may be considered as special type of orthotropic solid with three elastic constants. Sih described the relation between K_I and G_I for plane strain orthotropic solids in the form:

$$G_I = K_1^2 \left(\frac{b_{11}\, b_{22}}{2}\right)^{1/2} \left[\frac{b_{22}}{b_{11}}^{1/2} + \frac{2b_{12}+b_{66}}{2b_{11}}\right]^{1/2} \quad (19)$$

In which b_{ij} are the reduced elastic compliances for plane strain which are related to the original three dimensional elastic compliances as outlined by Sih (Sih et al., 1965):

$$b_{ij} = a_{ij} - \frac{a_{i2}a_{j3}}{a_{33}} \quad (20)$$

In which a_{ij} are the three dimensional elastic compliances which are related to the elastic constants by

$$[a_{ij}] = [C_{ij}]^{-1} \quad (21)$$

2.1.3 Developing Three Dimensional Models from Computerized Tomography 2D Image Slices:

Computerized Tomography, also called CT, is a series of X-ray images. These images are taken from different angles and combined together and cross sectional images are created. These cross sectional images help to visualize different parts of living bodies from different angles. When CT scan images are combined together they deliver a three dimensional surface geometry. This

surface geometry can be viewed around different axes of rotations. A three dimensional geometry can be created from the surface obtained.

In this study the CT scan images obtained were extracted from micro CT scan machines, where the resolution of the scanned images was as high as in micro scale. Micro CT images are typically used for analyzing small objects like small animal bodies, small body parts, biomedical samples and research studies. To observe the inner part of human bones and bones of other animals' micro CT scan images are used. To study the morphology of the spongy part of bone several CT scan data were obtained from different research labs where they have micro CT scan systems.

The series of two dimensional CT scan image slides were reconstructed by aligning and defining the region of interests (ROI). In this study three different types of micro CT scan images were used:

I. One 61 year old male human femoral neck: This series of CT scans were obtained from an online research community called Biomedtown. The images were reconstructed and three different models were created with three different densities by varying density of solid struts.

II. Artificially stimulated osteoporotic femur of young laboratory rats (C57/B6): Four CT scan series were obtained from Dr. Christopher Chen, UT Southwestern medical center. Among these samples three were scanned from fresh laboratory rat bone and the other was a frozen sample.

III. 6 months old pig femoral head, raised under diets satisfying appropriate nutrient levels. These samples were obtained from Dr. Iwona Jasiuk, University of Illinois at Urbana-Champaign.

From all the CT scan sets the trabecular part was separated and converted into three dimensional models for further finite element analysis. A set of predefined processes was followed to convert the CT scan images into three dimensional solid volume mesh. The program NRecon was used to correct the greyscale and long axis shift.

Medical image processing software MIMICS was used to combine the corrected two dimensional images and create a surface. The surface was observed and the effective ROI was chosen by defining threshold mask from the grey scale area. The selected mask was converted to three dimensional surfaces. The surface files were exported to Stereo lithography format for simplifying the outer surface curves. This file format contained the surface information of the geometry. Finite element preprocessor software was used to process the surface file. The .stl surface file was imported to the preprocessor software. In this software the surface file was cleaned by removing the floating objects. The cleaned surface geometry was meshed with area surface elements with a defined element length. Once the area mesh was done, it was converted to volume mesh. The volume mesh was done by four node tetrahedron elements. The four node tetrahedron mesh was converted to ten node tetrahedron mesh. The mesh file was then exported as input file for finite element program ANSYS.

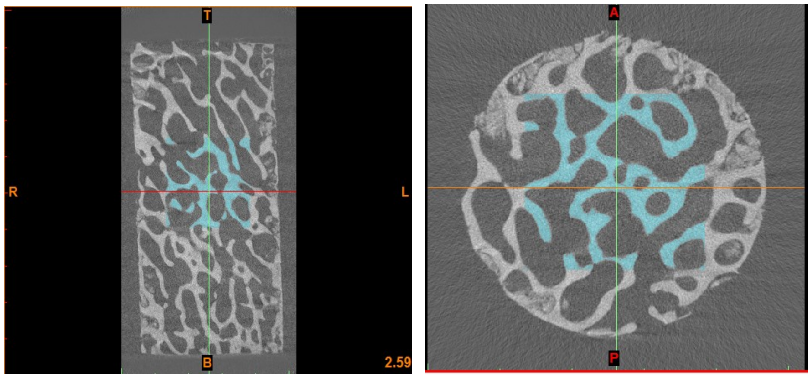

Figure 2-2 (a) Side view (b) of trabecular bone obtained from a pig femoral neck

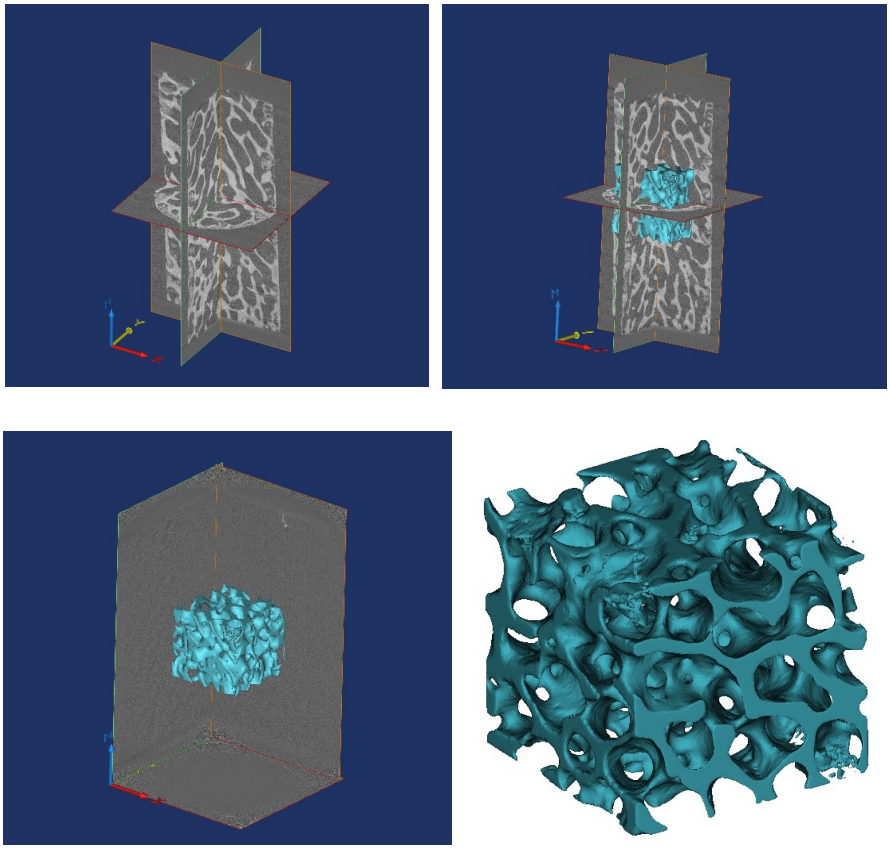

Figure 2-3 Merged cross sections of pig femoral neck and obtained trabecular geometry from selected region of interest

2.1.4 Developing Three Dimensional Approximated Structures to Represent Cancellous Bone Structure:

In this study the spongy part of bone was analyzed. The spongy part of the bone is also called trabecular bone or cancellous bone. Trabecular bone has numerous large spaces filled with bone marrow which makes it flexible. This part of bone has a larger surface to mass ratio. The porous structure of cancellous bone takes place inside the cortical bone. Trabecular bone is made up from the combination of irregular columns and struts. The column formation is totally random creating hollow spaces and of different diameters. Manmade structure that resembles trabecular bone had been studied for a long time. Here five different microstructures are created with three different densities to vary the apparent density.

These structures were assembled together and a porous structure was made. Each microstructure had a basic geometry of their own kind. A CAD software was used to generate the base geometry. This solid geometry was the converted into shell geometry leaving a circular hole at each face of it. The thickness of the shell was varied. Three shells were created naming thin, thick and medium. These hollow shell three dimensional models has solid bodies with hole, having an effective solid density and the solid density assuming there was no hole and the hollow part was filled with solid. The ratios of these two densities accordingly are called apparent density.

The hollow shell structures were combined together and an assembly was created with a constant edge length or hole diameter. Later these microstructures were subtracted from a solid cuboid shell to give all the microstructures a constant length and height. All the microstructures were 3mm in length and height.

2.1.5 Meshing and Elements:

The trabecular bones were meshed with the FEA meshing software 3-Matics. All the biological models, obtained from CT scan surfaces, were meshed using surface mesh in the program. The surface mesh was converted to volume mesh which is by default four node tetrahedron element. This mesh was then converted to ten node tetrahedron element mesh.

The other five microstructures were meshed in ANSYS with solid 187 element which is ten node tetrahedron elements. A balanced mesh was done on all the models, the number of elements were kept consistent for all the models. A mesh convergence study was done to determine the estimated number of elements which is converged and gives a stable FEA result. All the models had a length of 4mm to 2.5mm and they were meshed with eighty thousand to one hundred thousand elements.

Ten node tetrahedron elements are well suited for geometries of irregular surfaces. This element is capable of using anisotropic properties. In this study the general input property was transversely isotropic, so this element is perfect for this study.

Ten node solid tetrahedron elements have three translational degrees of freedom at each node. This element's large deflection and strain bearing capability was used in FEA.

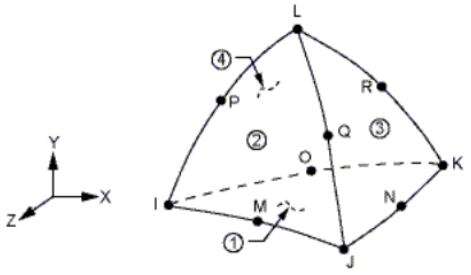

Figure 2-4 Ten node tetrahedral element (mid nodes shown)

2.2 Overview of the Models:

2.2.1 Trabecular Bone FEA Models

2.2.1.1 Human Femoral Neck

Reconstructed 2D slices of Micro CT scan series of a human bone biopsy taken from the femoral neck of a 61 year old male were collected. Region of interest (ROI) was pre extracted into a 4mm x 4mm x 4mm volume of interest (VOI). Reconstruction program was used to fix z axis shift and x-y axis alignment of the scanned images.

Mimics was used to edit the threshold of the ROI. A volume was created from the ROI using default mask properties of cancellous bone. Ten node tetrahedron elements were used to create a three dimensional volume mesh. Eight different meshes were created with different element numbers until a mesh convergence was reached.

Table 2-4 Human Femoral Neck Trabecular geometry properties

Type of model	Volume of solid extracted	Dimensions	Apparent density
Thin	7.9345 mm^3	4x4x4 mm	0.21 g/cm^3
Original	9.215 mm^3		0.26 g/cm^3
Thick	21.012 mm^3		0.59 g/cm^3

This three dimensional model was created using three different thresholds and smoothening properties in the reconstructing stage. As a result three different trabecular cubes were found with three different thickness and different relative densities. Pre-decided loading conditions in FEA for quarter model linear elastic solution were applied. Each of these models was assumed to have a crack along all the three axes. In total nine FEA simulations were done to compare the results. Fracture toughness was calculated using transversely isotropic material properties.

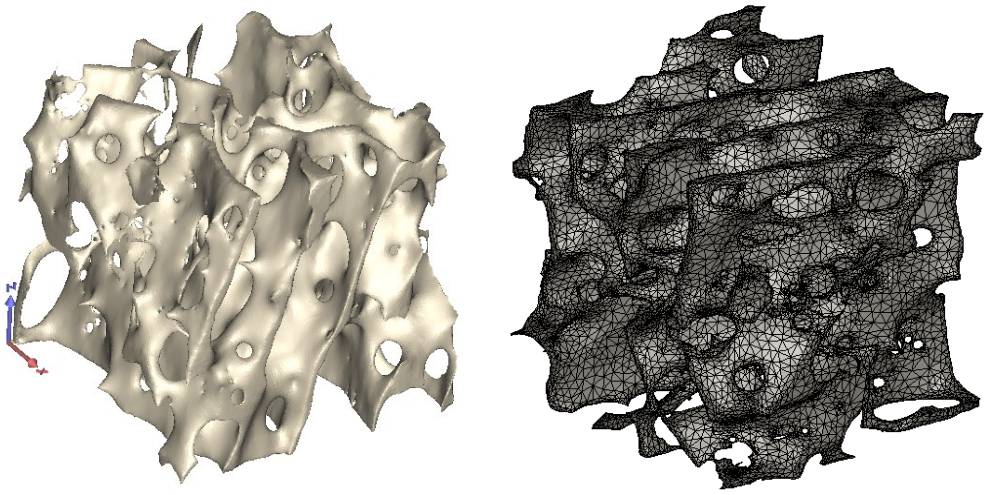

Figure 2-5 (a) 3D Solid model (b) Meshed model of Human femoral neck trabecular structure.

2.2.1.2 Pig Femoral Neck

Five different pig femoral neck micro CT scan data were obtained. All the pigs were 6 months old (Sus scrofadomestica) and all of them were healthy, raised under diets satisfying appropriate nutrient levels.

All the scans were conducted on the femoral neck. The resolution of all the images was 10umx10umx100um. Among the five micro CT data one had been frozen and the other four were fresh sample at the time of scan. The obtained data were cylinders of 4mm diameter and 8mm long. To avoid cylindrical coordinate system a region of interest (ROI) chosen was a cube with a side length of 2.5mm.

The ROI of each model was generated using a consistent threshold value and a consistent method of smoothening. Within the five different femoral neck scans, the frozen models had the highest solid volume.

Table 2-5 Pig femoral neck trabecular geometry properties

Type of scan	Volume of solid extracted	Dimensions	Apparent density
Frozen sample	6.419 mm^3	2.5x2.5x2.5 mm	0.74 g/cm^3
Fresh sample-1	5.668 mm^3		0.65 g/cm^3
Fresh sample-2	6.356 mm^3		0.73 g/cm^3
Fresh sample-3	3.606 mm^3		0.41 g/cm^3
Fresh sample-4	4.011 mm^3		0.46 g/cm^3

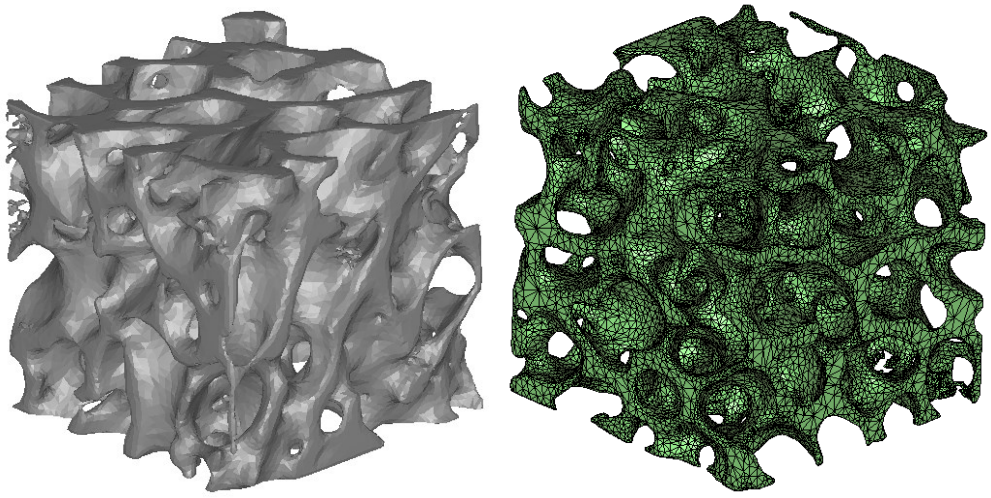

Figure 2-6 (a) 3D Solid model (b) Meshed model of pig femoral neck trabecular structure.

2.2.1.3 Rat Femoral Head

Four rat femur micro CT scan images were obtained. All the rats were artificially stimulated with osteoporosis. These samples are femurs from genetically modified mice (C57/B6) which is used in laboratory for stimulating human diseases. The animal #688L is a GPR30-knockout animal. 692L is wild type (GPR30+) animal and was induced for osteoporosis for about 6 weeks by

OVX. Both 690L and 691L are wild type animals. Region of interest was selected from femoral head from the complete femur as this part showed the maximum formation of trabecular bone.

Table 2-6 Rat Femoral head trabecular geometry properties

Type of model	Volume of solid extracted	Dimensions	Apparent density
Sample-1(688L)	0.1215 mm^3	0.6x0.6x0.6mm	1.012 g/cm^3
Sample-2(690L)	0.12 mm^3		1.0 g/cm^3
Sample-3(690L)	0.041 mm^3		1.15 g/cm^3
Sample-4(691L)	0.003 mm^3	0.08x0.08x0.08mm	0.58 g/cm^3

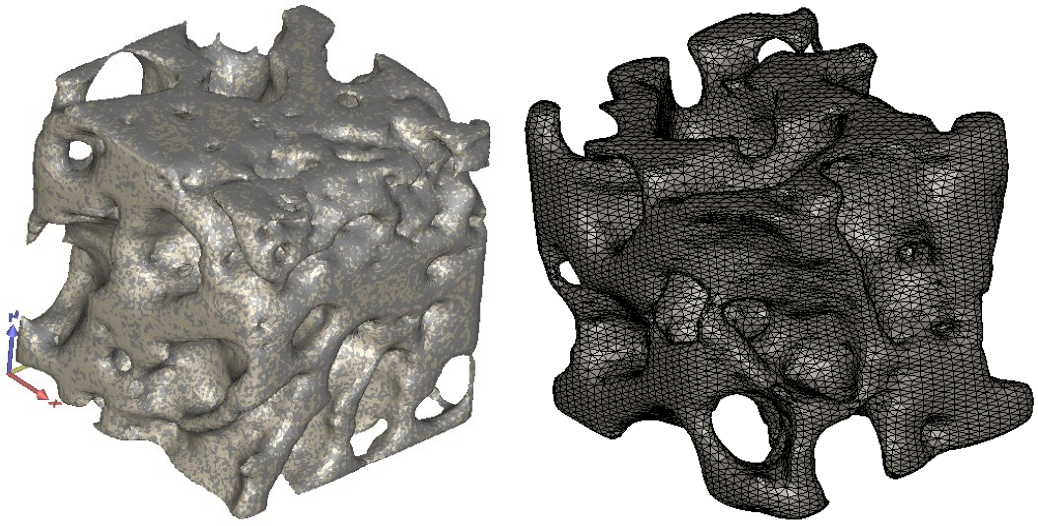

Figure 2-7 (a) 3D Solid model (b) Meshed model of rat femoral head trabecular structure

2.2.2 Approximated Three Dimensional FEA Models

The structure of cancellous bone is cellular solid like many other materials. All these structures are able to support large loading conditions over the period of times. An increasing need for replacing fractured bone with manmade artificial microstructures leads to study the similarity and applicability of different microstructures. The load bearing structural properties of microstructures vastly depend on the density and efficient packaging of cellular solids.

In this research we focused on different types of unit cells and their dimensions. These cells are made from interconnected struts. There are different types of cell structures with struts and plates. Those foams which are connected with struts that define edges are called open foams. Those structures which are connected with plates are called closed cell structures. In this study only open cell foams are analyzed.

One of the most important properties of cellular solids is relative density. Relative density is the measure of lightness or thickness of a cellular material. Relative density of cellular solid depends on the thickness, length of unit strut, hole size of open cell foam structures.

There are different types of three dimensional polyhedral cells. Among those cells triangular prism, rectangular prism, hexagonal prism, rhombic dodecahedron and truncated octahedron are the ones which can be efficiently packed in three dimensional spaces.

2.2.2.1 Triangular Prism

Triangular prism has five sides. A unit of a triangular prism is made of two triangular faces and three rectangular faces. It's created from the three dimensional extrusion of an equilateral triangle. In three dimensional space triangular prisms are packed by connecting the triangular faces together and the rectangular faces together. In this study this polyhedron was made as an open cell foam unit cell by removing a circular space form each of its faces. The triangular faces can fit a smaller circle than the one on the rectangular face. Hence to create an open cell foam two different extruded circles were subtracted from the faces of each units, maintaining a ratio to their thickness. The units were maintained with a consistent strut length. After subtracting the extruded circles or

cylinders from each faces a shell was created with a random meaningful thickness. The model was then converted to parametric one and the thickness was varied to create three different thicknesses and relative densities. This open cell triangular prisms were connected together by matching the faces and strut lengths. Finally a solid hollow cube was subtracted from the assembly to achieve a cubic shape with open struts on each sides. This assembly was then meshed with tetrahedron ten elements for further finite element analysis.

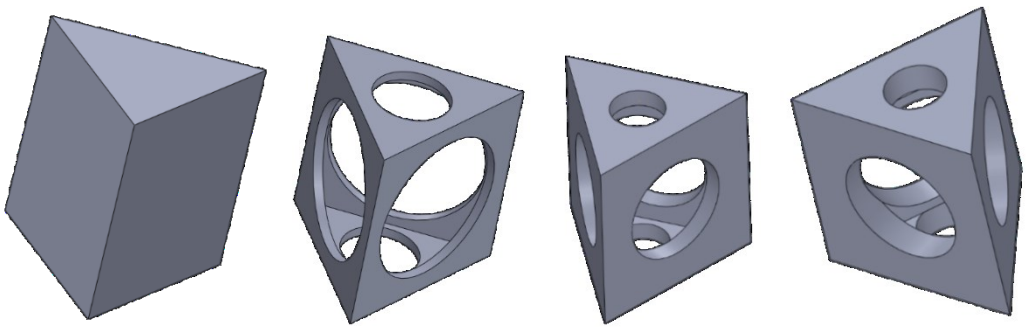

Figure 2-8 Triangular prism : Solid, thin shell, intermediate shell and thick shell

Table shows the dimensions used for creating different thickness of triangular prisms. The column “volume of solid” refers to the volume of assemblies.

Table 2-7 Dimensions and geometrical properties of triangular prism

Thickness	Unit hand length	Hole diameters	Shell thickness	Dimensions	Volume of solid	Relative density
Thin	1mm	0.8mm/0.4mm	.05mm	3x3x3mm	2.48mm^3	0.16 g/cm^3
Intermediate	1mm	0.6mm/0.3mm	.1mm	3x3x3mm	6.88mm^3	0.46 g/cm^3
Thick	1mm	0.6mm/0.3mm	.17mm	3x3x3mm	7.62mm^3	0.51 g/cm^3

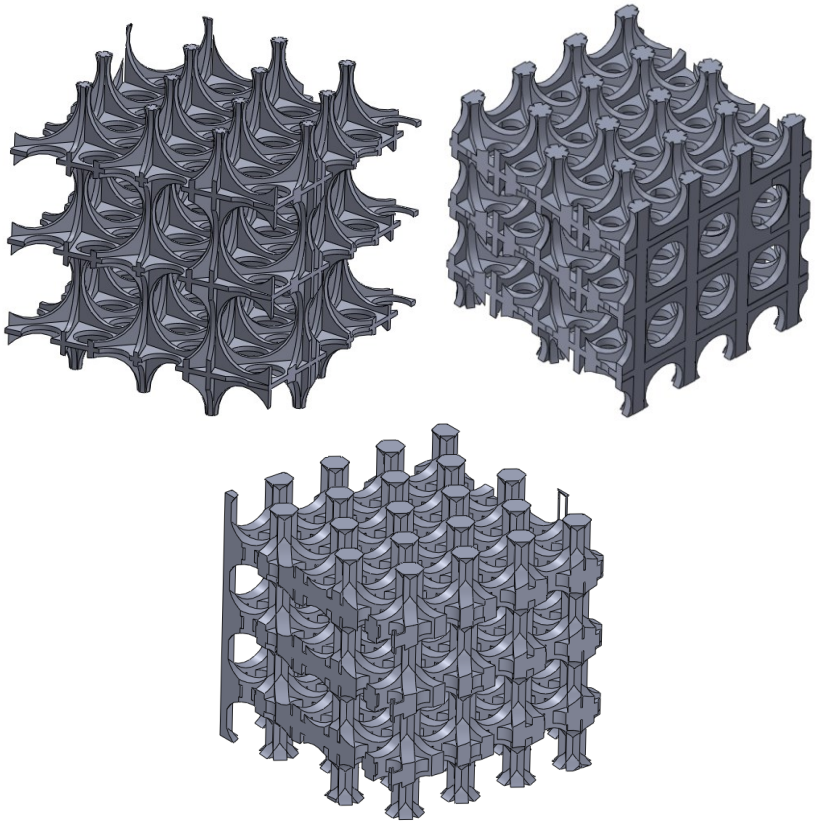

Figure 2-9 Assemblies of triangular prism unit cells

2.2.2.2 Rectangular Prism

Rectangular prism is combined of six faces. Cuboid is a special case of rectangular prism where all the faces have same surface area or hand lengths. Rectangular prism is one of the three dimensional cells which can be easily packed efficiently. These prisms can be packed by connecting one face to another and overlapping the common volume, creating a single wall between them. In this study a cuboid was given a shape of an open cell by subtracting cylinders which from each walls. In this case the hole diameter was kept consistent with a varying unit strut length. Along with the strut length the thickness of shell was changed from low to high and three different thickness

was achieved. These unit open cells were connected and three assemblies were created with three different apparent density. These assemblies were meshed with tetrahedron ten elements.

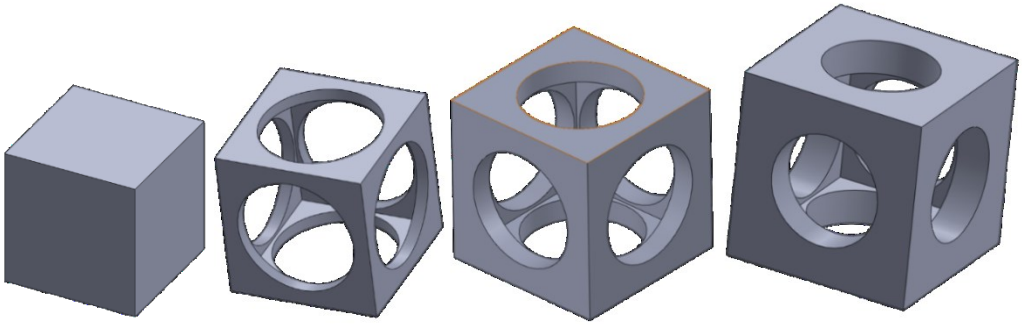

Figure 2-10 Rectangular prism: Solid, thin shell, intermediate shell and thick shell

Table 2-8 Dimensions and geometrical properties of rectangular properties

Thickness	Unit hand length	Hole diameters	Shell thickness	Dimensions	Volume of solid	Relative density
Thin	0.5mm	0.4mm	.04mm	3x3x3mm	1.9mm^3	0.13 g/cm^3
Intermediate	0.57mm	0.4mm	.07mm		4.18mm^3	0.28 g/cm^3
Thick	0.67mm	0.4mm	.12mm		6.1mm^3	0.41 g/cm^3

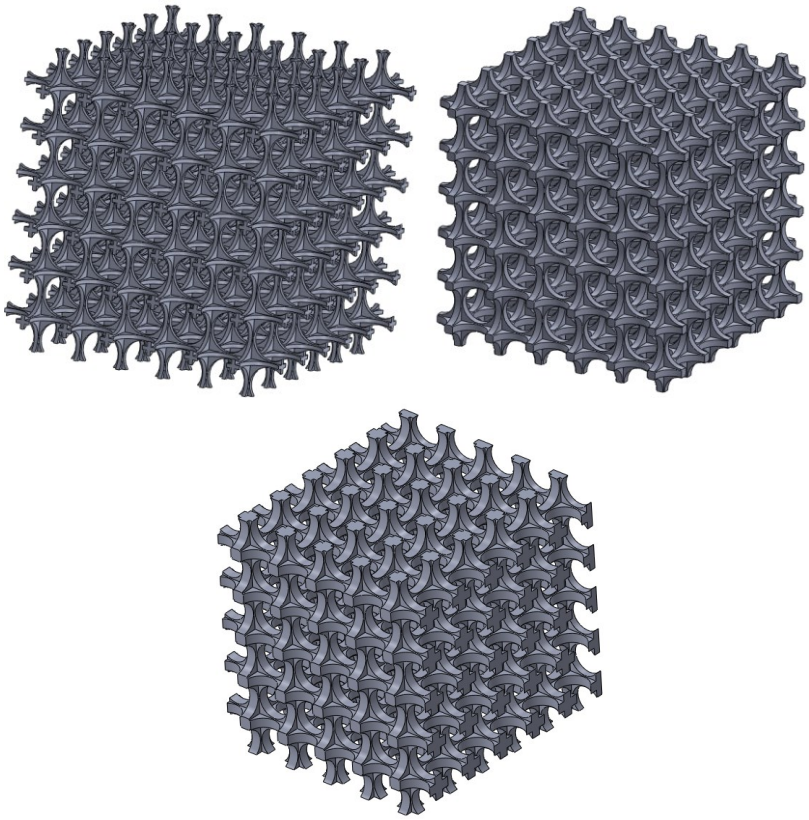

Figure 2-11 Assemblies of rectangular prism unit cells

2.2.2.3 Hexagonal Prism

Hexagonal prism has eight faces with hexagonal top and bottom faces. Hexagonal prism can be obtained by extruding a two dimensional equilateral hexagon. It has six rectangular sides and two hexagonal sides. It can be packed efficiently. Hexagonal prism can be converted to an open cell foam by subtracting circular cylinders from the hexagonal faces. To maintain a uniform shape the side faces has to be rectangles to match the hexagonal diameter with the height. Elliptical cylinders were subtracted from the rectangular faces. The top and bottom circular holes were kept consistent in dimension and all other dimensions were changed to achieve three different thickness. Three assemblies were created using three different unit cells. Ten node tetrahedron elements were used to mesh all the assemblies.

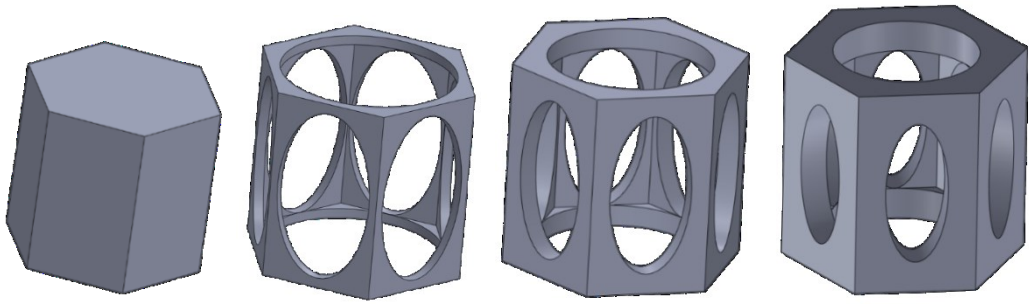

Figure 2-12 Hexagonal prism: Solid, thin shell, intermediate shell and thick shell

Table 2-9 Dimensions and geometrical properties of hexagonal prism

Thickness	Unit hand length(mm)	Hole diameters (mm)		Shell thickness	Dimensions (mm)	Volume of solid	Relative density
Thin	0.26mm	0.4	0.4/0.2	.05mm	3x3x3	1.73mm^3	0.11 g/cm^3
Intermediate	0.3mm	0.4	0.4/0.2	0.1mm	3x3x3	4.7mm^3	0.31 g/cm^3
Thick	0.33mm	0.4	0.3/0.15	0.17mm	3x3x3	8.68mm^3	0.58 g/cm^3

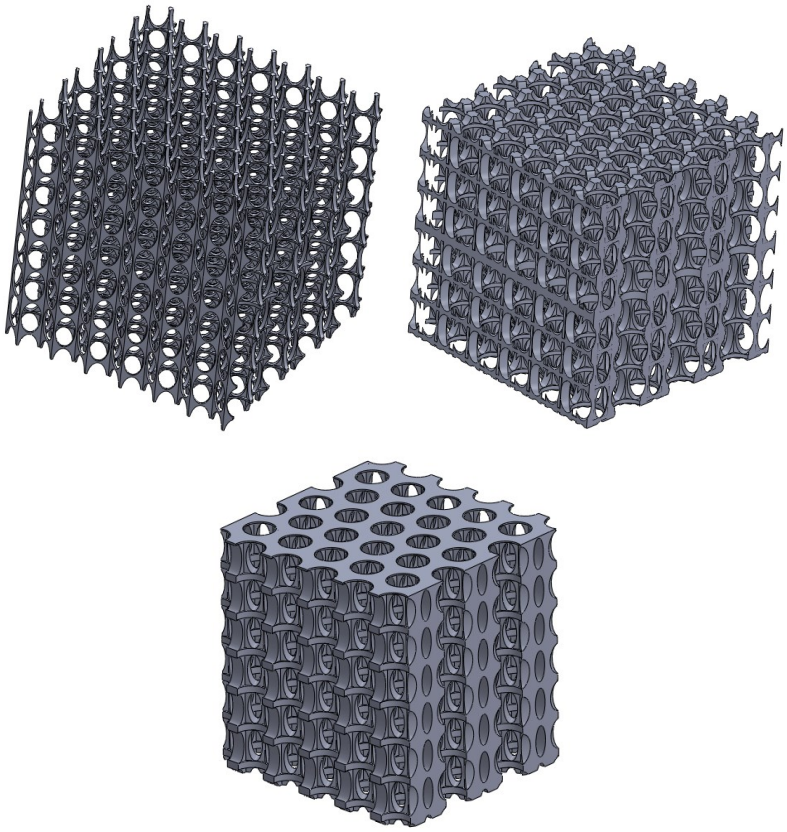

Figure 2-13 Assemblies of hexagonal prism unit cells

2.2.2.4 Rhombic Dodecahedron

Rhombic dodecahedron is a polyhedron with twelve rhombic faces of two types. Eight of them are of similar dimensions and the rest of four are identical. An open cell foam structure can be achieved from this tetrahedron by removing extruded circles of two sizes from all the faces. There are two types of rhombic faces in this unit cell, the group of four and the group of six due to a difference in angles. It was seen that the group of four has a slightly less circumference than the group of six. Hence the circular removable areas have two different diameters. In this case keeping the unit rhombus length and cylinder diameter consistent only the thickness of the shell was

changed. Three different unit cells were created of different thickness. The assembly was created and was meshed with ten node tetrahedron elements.

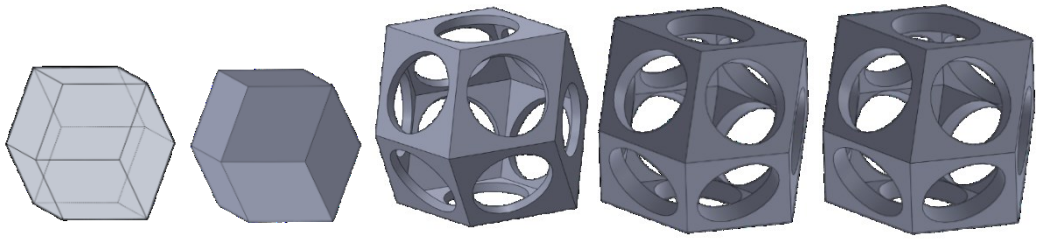

Figure 2-14 Rhombic dodecahedron: Solid, thin shell, intermediate shell and thick shell

Table 2-10 Dimensions and geometrical properties of rhombic dodecahedron

Thickness	Unit hand length(mm)	Hole diameters(mm)	Shell thickness	Dimensions	Volume of solid	Relative density
Thin	0.61/0.56	0.46/0.4	.05mm	3x3x3mm	3.0mm^3	0.2 g/cm^3
Intermediate	0.61/0.56	0.46/0.4	.08mm	3x3x3mm	3.98mm^3	0.27 g/cm^3
Thick	0.61/0.56	0.46/0.4	.1mm	3x3x3mm	5.38mm^3	0.36 g/cm^3

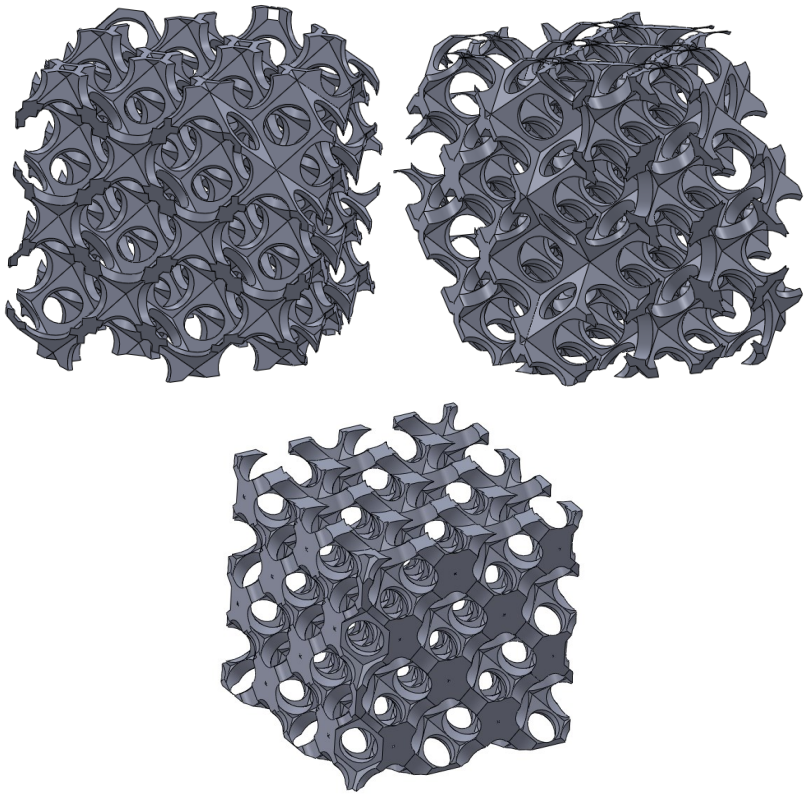

Figure 2-15 Assemblies of triangular prism unit cells

2.2.2.5 Truncated Octahedron

Truncated octahedron is a three dimensional unit cell having fourteen faces. Among the fourteen faces eight faces are hexagons and six faces are squares. This unit cell is also called Tetrakaidecahedron. An open cell structure was achieved by removing circular area from each faces. These unit cells can be easily packed by matching the faces geometry and overlapping the common wall. Two different circular area was subtracted from each faces and an open cell was created. In this case a consistent unit hand length was maintained and the hole diameter was changed keeping the same shell thickness. These unit cells were assembled together and were meshed with ten node tetrahedron elements.

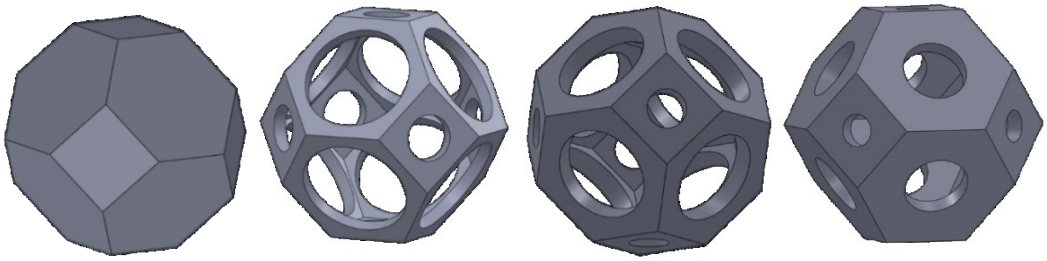

Figure 2-16 Truncated octahedron: Solid, thin shell, intermediate shell and thick shell

Table 2-11 Dimensions and geometrical properties of truncated octahedron

Thickness	Unit hand length(mm)	Hole diameter (mm)	Shell thickness	Dimensions (mm)	Volume of solid	Relative density
Thin	0.38mm	0.53/0.23	.1mm	4x4x4	5.13mm^3	0.16 g/cm^3
Intermediate	0.38mm	0.45/0.19	.1mm	4x4x4	8.21mm^3	0.46 g/cm^3
Thick	0.38mm	0.3/0.15	.1mm	4x4x4	10.5mm^3	0.51 g/cm^3

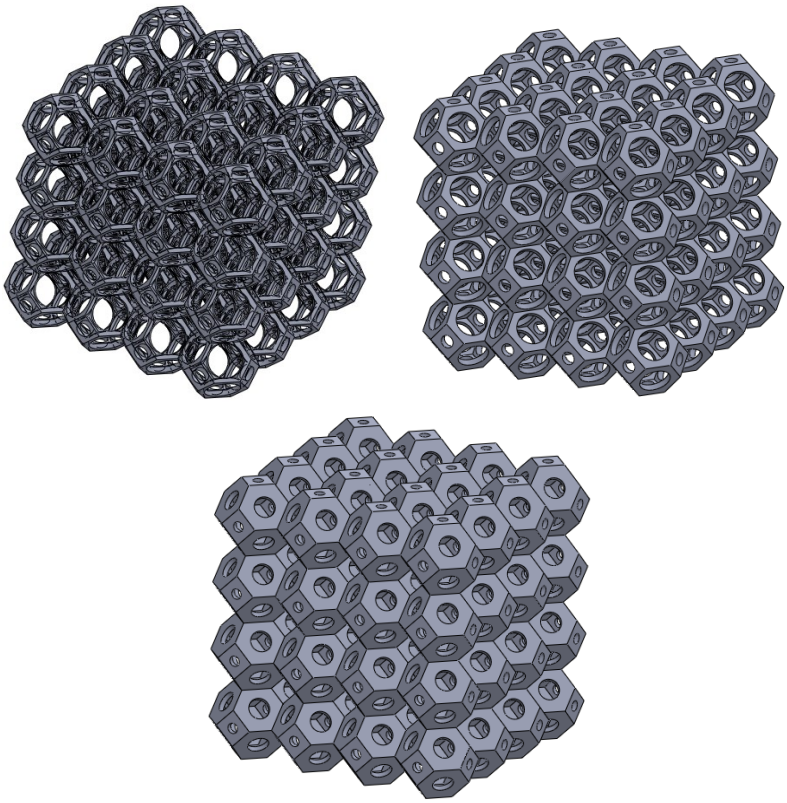

Figure 2-17 Assemblies of truncated octahedron unit cells

Chapter 3

Effect of Density on Fracture Toughness of Cancellous Bone

Fracture toughness is an important property to characterize material quality. The property fracture toughness is related to the value of stress intensity factor of a structure. At a certain value of stress intensity factor the line crack starts to grow which is called the critical stress intensity factor as well as the fracture toughness which is denoted by K_{IC}. Fracture toughness is highly dependent on the elastic properties of the material. To study the mechanical behavior, degradation mechanics and the microstructural diagnostic the study of fracture toughness is very important.

There are two basic methods to approximate the value of fracture toughness, one of them is the measuring of the critical stress intensity factor. For porous solid structures a measure of its effective volume is apparent density. Apparent density is calculated as the mass per unit real volume.

The material properties of trabecular bone and foam like materials depend highly on the density. There are several ways to define the density of porous materials. In this study the density was defined as the apparent density which is the ratio of occupied volume and total volume with void, multiplied by tissue density which is $1.8 g/cm^{-3}$.

For estimating fracture toughness the modified crack closure method was used. This method is executed by recording the maximum stress at the crack tip. Due to geometrical complexity the definition of crack tip and collecting the values at different nodes was followed by certain procedures. To avoid edge effect the bottom of the trabecular bone models were fixed at a certain distance along the axis of applied load at the top. For each model the top part was selected in the same way as the bottom part. Tensile strain was applied at the selected nodes on the top part and the bottom part was fixed at all selected nodes. It was assumed as a quarter simulation.

3.1 Human Bone

A sample of human trabecular bone was collected to conduct the fracture toughness study related to the apparent density. The model was built from a micro CT scan image series. Three different densities were extracted from the single micro CT scan image set by varying thickness. The original thickness was lessened and was named thin and the thick model was achieved by increasing the thickness.

For all the human trabecular models the longitudinal axis was the z axis, the x and y axis were transverse. Apparent density was varied with the varying occupied volume. The original model had osteoporotic tendency hence thickening was more convenience than lessening the volume. The final values of the apparent density came out to be in a range from 0.2 g/cm^3 to 0.6 g/cm^3.

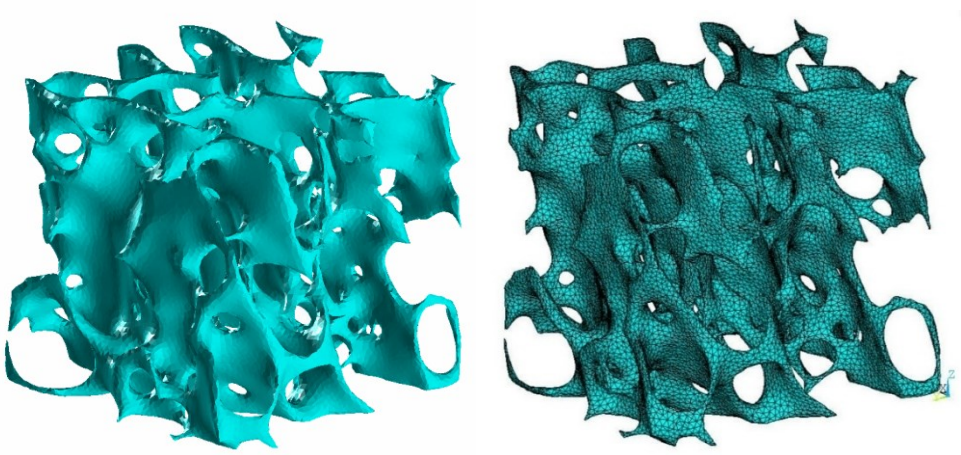

Figure 3-1 Three dimensional and meshed trabecular bone

The yellow color at the top of the model indicates applied displacement boundary condition. The yellow at the bottom indicates the fixed boundary condition in all degrees of freedom. Half of the bottom plane was fixed and half was left free. The free part of the bottom plane resembled crack.

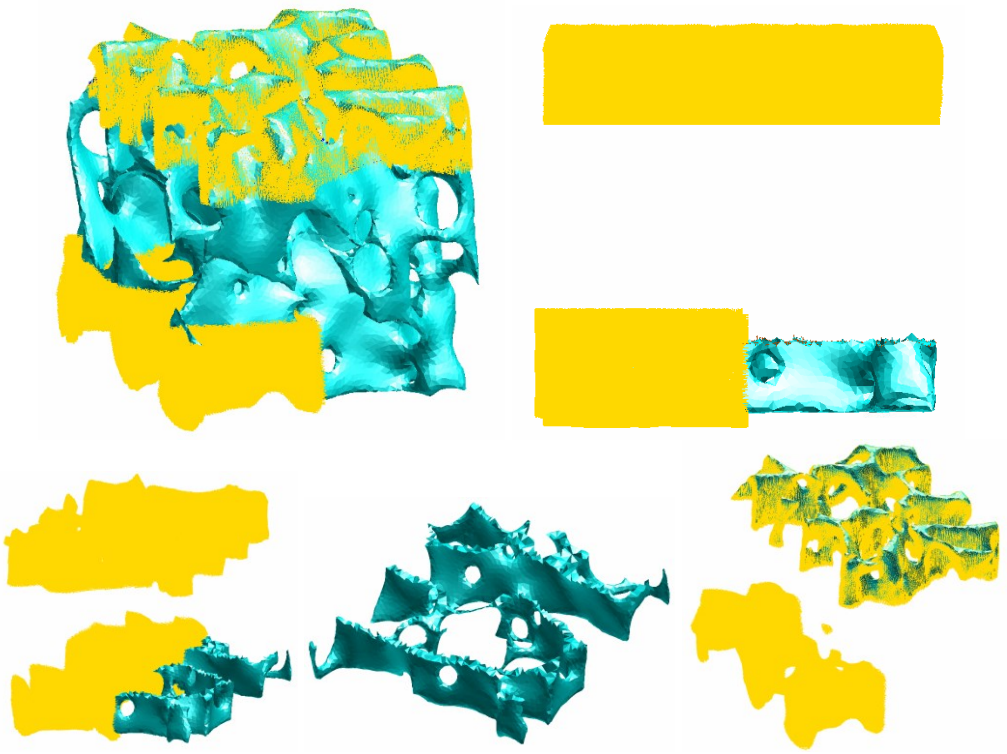

Figure 3-2 Different views of loaded trabecular bone with strain

A cross section of all the three different models is shown. This cross section plane is the plane from where the maximum crack tip was collected. With varying apparent density the thickness of the occupied area is visible. With increasing thickness the voids are filled up by solids creating stronger struts and connecting bodies.

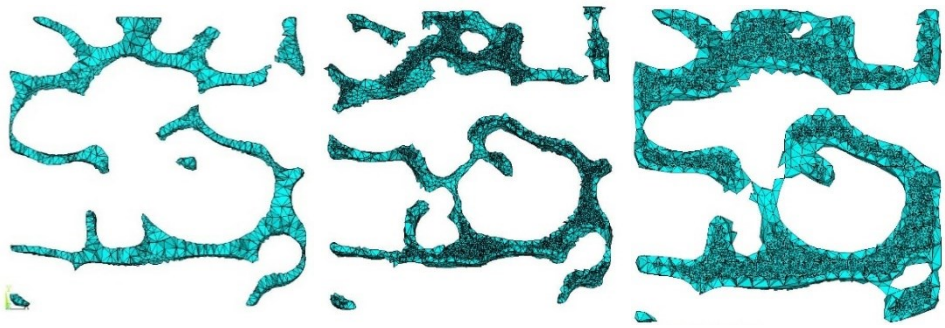

Figure 3-3 Cross section of result collection plane of three human femoral neck trabecular bones with three different apparent densities

The average effective stress was collected from ahead of the crack tip towards fixed part. The cross section shows the surface of the plane from where the effective stress values were collected. The displaced nodes were selected from a distance from the fixed line towards the free end. The coordinate values of these nodes were recorded along with the displaced values along the axis of tensile load.

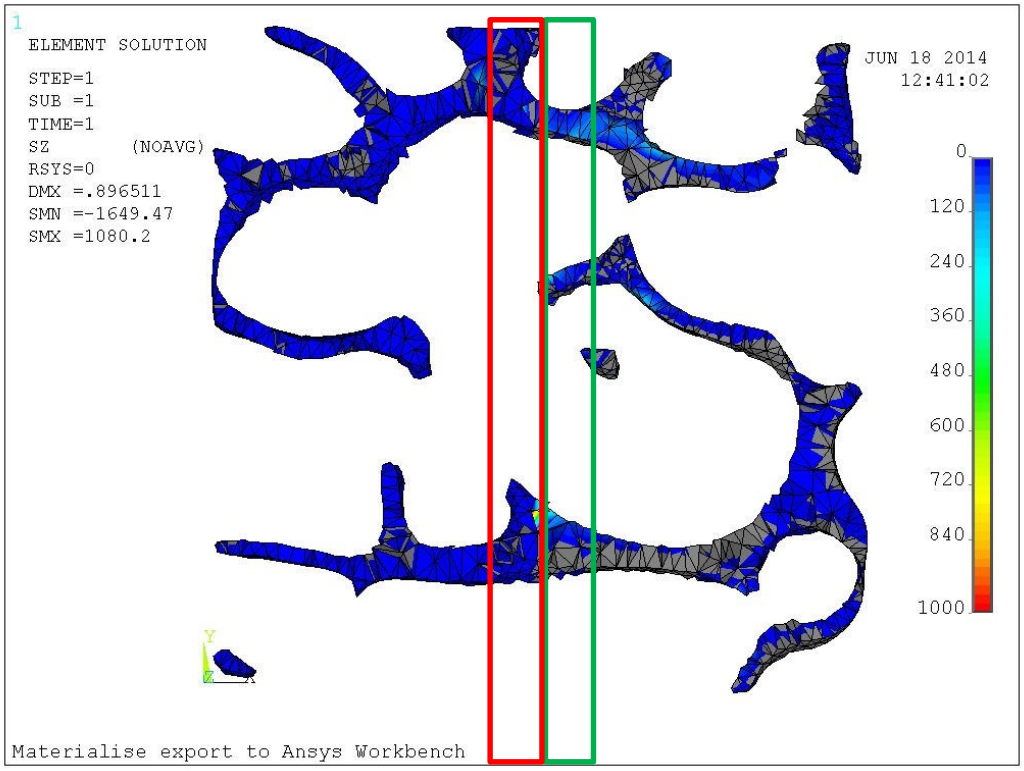

Figure 3-4 Deformed cross section after FEA simulation: Average stress and force was collected from the red part and displacement was collected from the green part bounding box

The table shows the values of fracture toughness obtained for the corresponding models. In all the models of human femoral neck trabecular bone the longitudinal axis was the z axis and the transverse axis were the other two axis.

Table 3-1 Fracture toughness of human trabecular bone

Crack along	Apparent density	Fracture toughness
Z-longitudinal axis	0.21	0.0083
	0.26	0.0176
	0.59	0.0624
X-transverse axis	0.21	0.014
	0.26	0.027
	0.59	0.0936
Y- transverse axis	0.21	0.0125
	0.26	0.024
	0.59	0.09

The results show that when the crack was placed at the transverse plane and the tensile load was applied to the longitudinal axis, the trabecular bone in all the three cases of densities showed less strength.

The critical stress intensity factor values for the three different densities were plotted and a trend line was found. The trend line for the crack placement in the transverse plane shows a linear increment in the values of fracture toughness and critical stress intensity factor. The value of coefficient of determination is nearly perfect.

For the first set of simulation the crack was placed along z axis in the x-z plane and the tensile loading was applied along one of the transverse axis y. The results showed the value of critical stress intensity factor increases linearly with increasing apparent density.

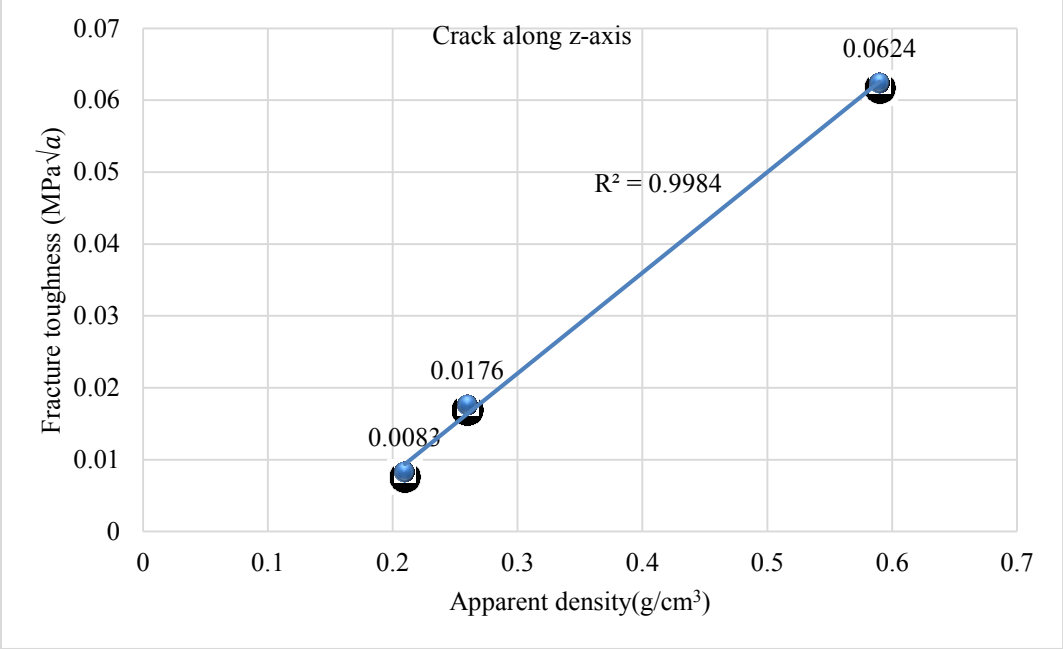

Figure 3-5 Apparent density vs. fracture toughness plot (crack along z axis)

The second set of simulations was done assuming the crack was along the y axis in the x-y plane. In this case tensile load was applied along the longitudinal axis z. The application of the boundary conditions were set as described previously in this chapter. The modified crack closure method was applied to calculate the fracture toughness or the critical stress intensity factor. The average of stress from a certain distance from the strut edges was collected to estimate the maximum stress value ahead of the crack tip. The displaced nodes after simulation were recorded vertically and horizontally.

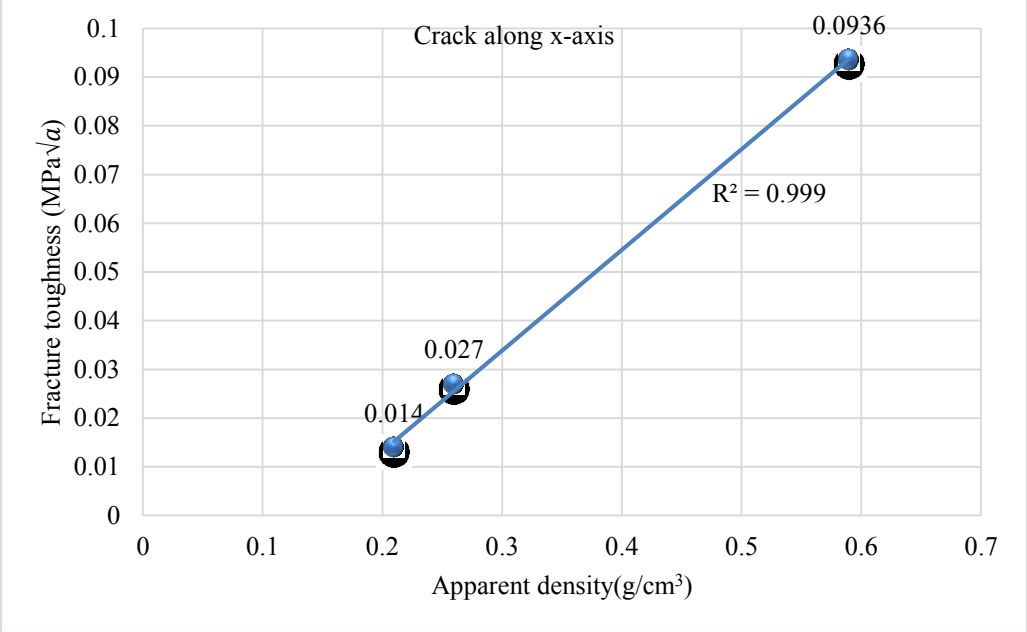

Figure 3-6 Apparent density vs. fracture toughness plot (crack along x axis)

The results were found to follow the similar trend line as the previous set of equations. The values of fracture toughness varied with apparent densities linearly.

The next set of simulation was done by assuming the crack along the y axis. In this case the crack was placed in the y-z plane and the longitudinal axis was the x axis. The results were similar to the previous sets.

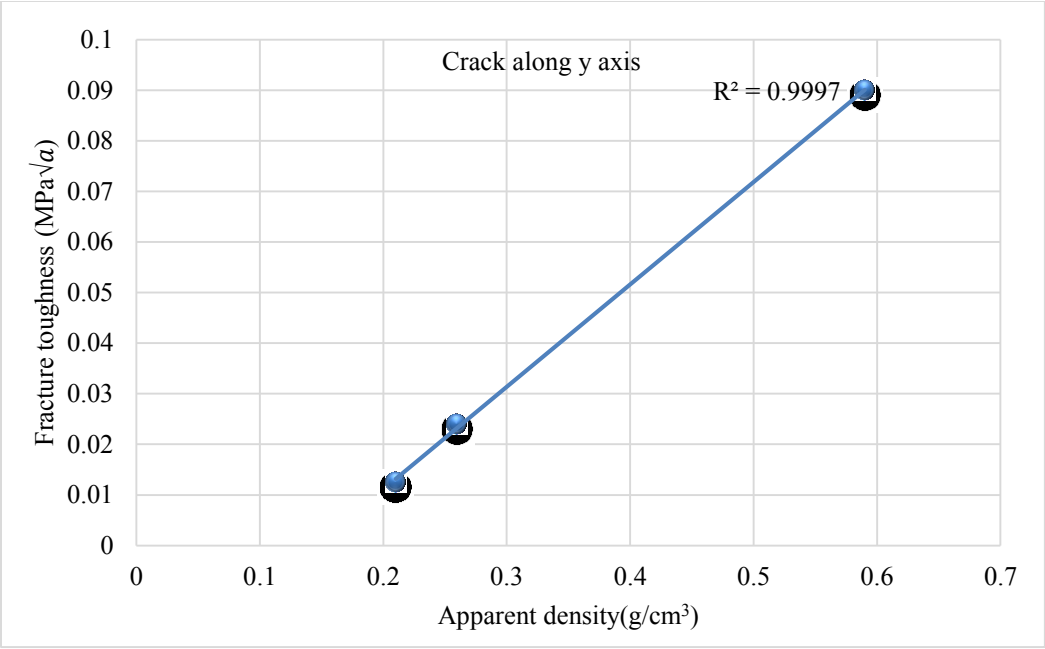

Figure 3-7 Apparent density vs. fracture toughness plot (crack along y axis)

Finally all the fracture toughness results were plotted in a single graph. A common trend line was found for all the nine simulations. This trend line is a rough estimation of the relation between fracture toughness and apparent density.

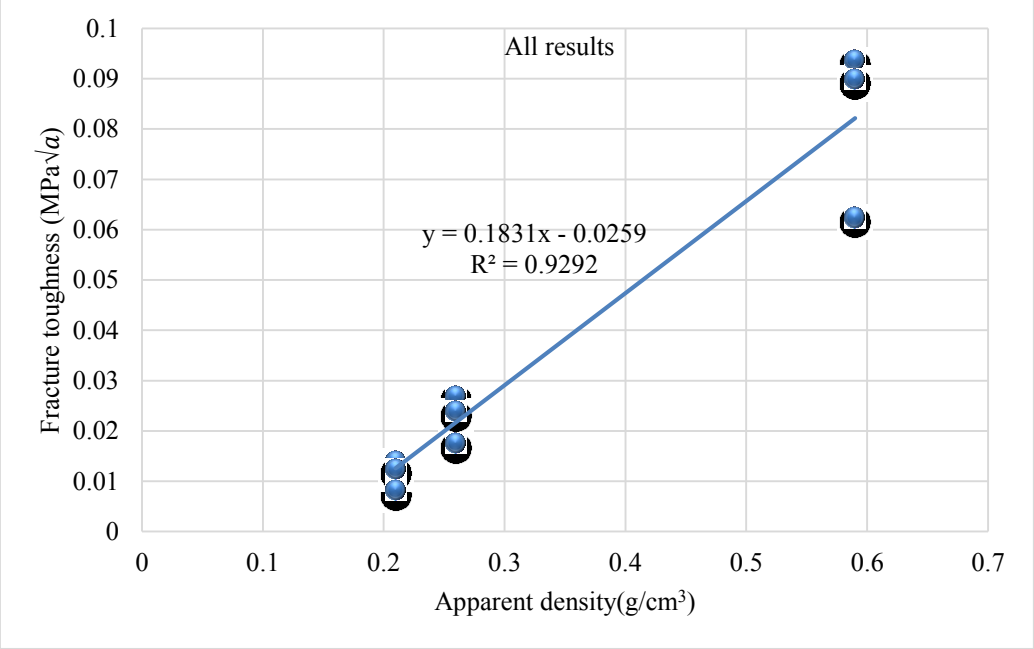

Figure 3-8 Apparent density vs. fracture toughness plot for all previous results

The trend line suggests that in general the value of fracture toughness is proportional to the apparent density of the trabecular bone. In this case for the human trabecular femoral neck trabecular structure the relation between apparent density and trabecular bone is:

$$Fracture\ toughness = (0.18 \times Apparent\ density) - 0.26$$

3.2 Pig Bone

Five samples of pig femoral neck was collected, four of them were scanned from fresh bone and the other one was frozen bone. All the samples were collected from healthy pigs kept in proper nutrition. From all the CT scans small cubes of 2.5mm length was extracted. Their apparent density varied from 0.42 g/cm^3 to 0.74 g/cm^3.

Table 3-2 Fracture toughness of pig trabecular bone

Apparent Density	Critical Stress Intensity Factor (K_{IC})
0.74	0.043
0.66	0.035
0.73	0.027
0.42	0.021
0.46	0.021

The cross sections are shown from where the maximum stress and the displacements from nodes were collected. The first model has the most dense surface and the results showed it had highest value of fracture toughness among the five models. The last three trabecular cross sections show weaker properties though one of them has good apparent density.

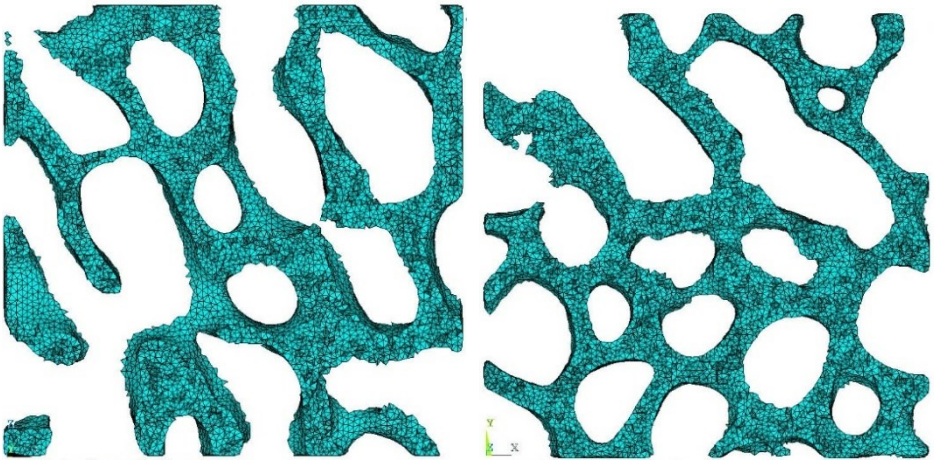

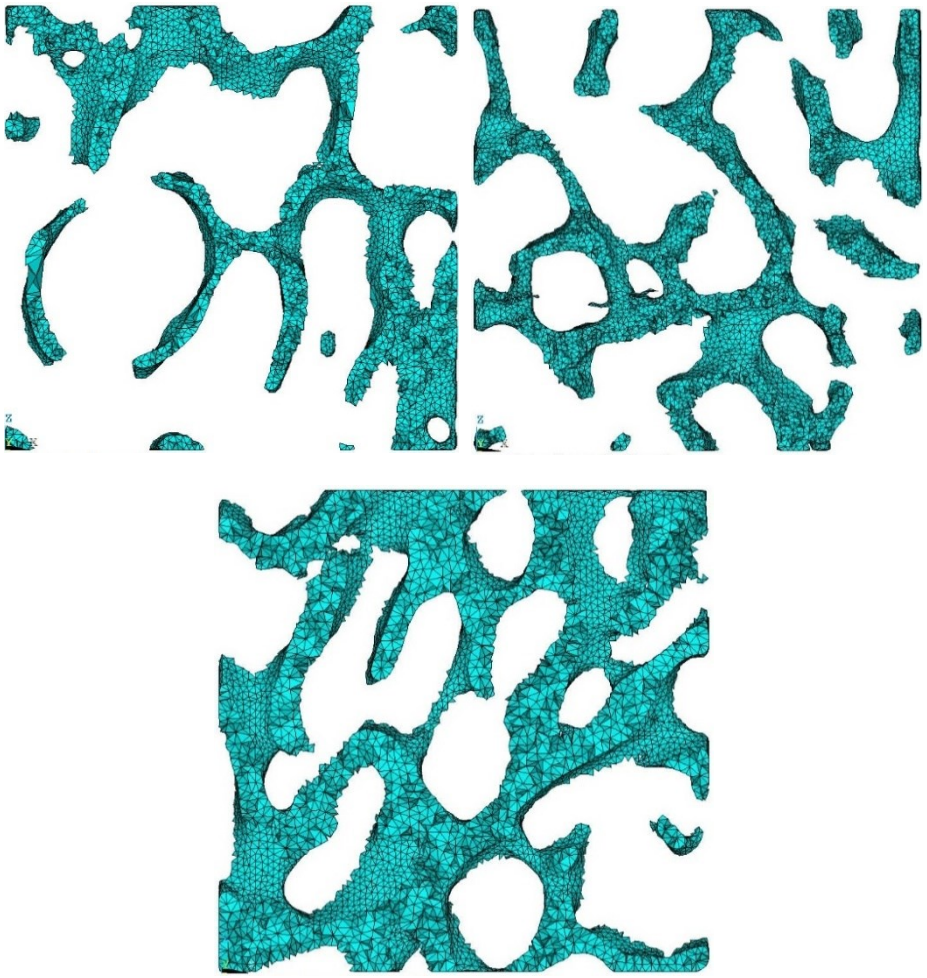

Figure 3-9 Cross section of result collection plane of five pig femoral neck trabecular bones with five different apparent densities

The trabecular structures showed similar results with the crack placed in different planes. For pig femoral neck trabecular bone the determination of longitudinal axis was not trivial by observation and results, hence for all the pig trabecular bone models the results from one plane is reported which resembles the other two planes as well.

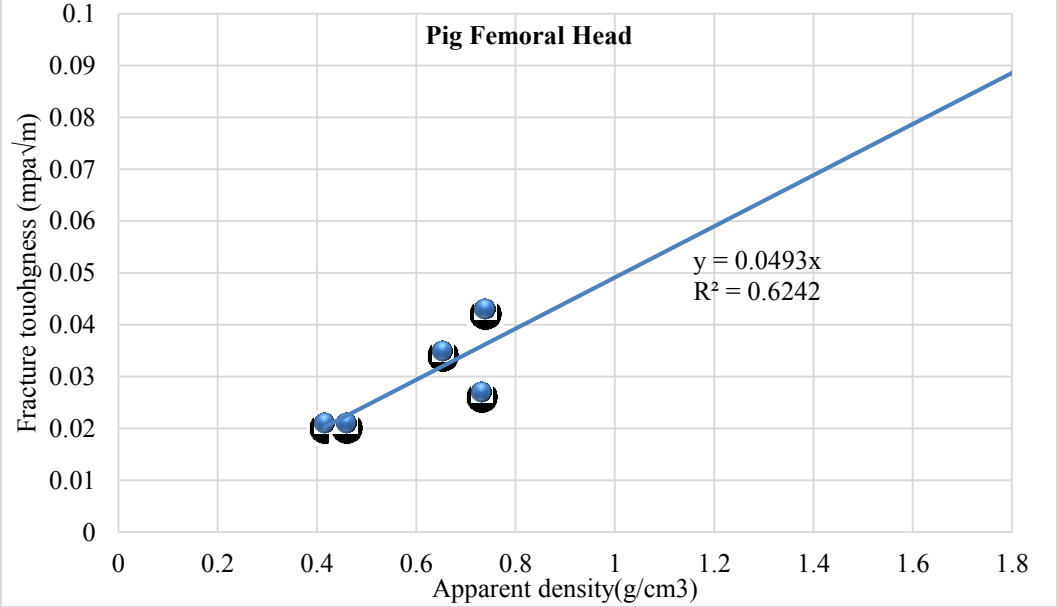

Figure 3-10 Fracture toughness vs. apparent density of pig trabecular bone

The critical stress intensity factor was plotted against the apparent density and the set of five simulations shows a trend. From the trend line a linear relation was estimated.

$$Fracture\ toughness = (0.05 \times Apparent\ density)$$

3.3 Rat Bone

The samples of rat trabecular bone were collected from rat femurs. These femurs were stimulated with osteoporosis artificially. The shaft of the femurs showed signs of osteoporosis but the femoral heads were dense enough to extract cubes of trabecular samples.

Apparent Density	Critical Stress Intensity Factor (K_{IC})
1.01	0.013
1	0.011
1.15	0.014
0.59	0.01

From all the collected rat bones only four of them were usable for analysis. Two of them show close apparend density, one shows a little higher and the other one is almost half of the others. For calculating fracture toughness the effective stress values were collected from the trabecular bone samples accordingly.

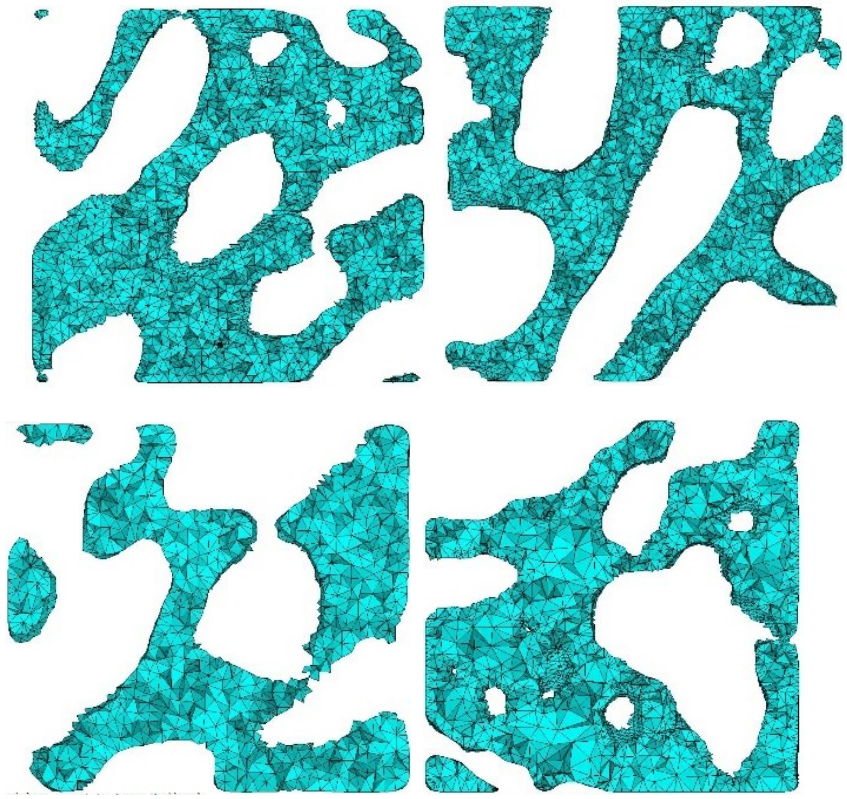

Figure 3-11 Cross section of result collection plane of four human femoral neck trabecular bones with four different apparent densities

The results were plotted and the four sets of data gives a trendline. From this trendline it can be seen that for the data from similar sets of trabecular bones of femoral head the relation between fracture toughness and apparent density follows the equation:

$$Fracture\ toughness = (0.0064 \times Apparent\ density)$$

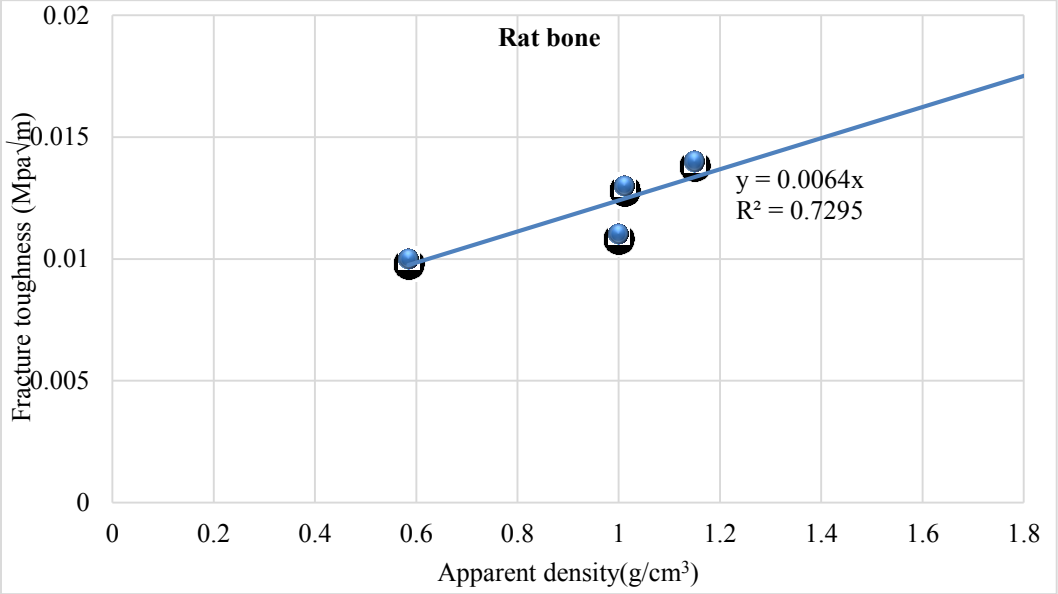

Figure 3-12 Fracture toughness vs. apparent density of rat trabecular bone

3.4 Comparison of All Trabecular Bones

In the fracture toughness study three types of trabecular bone were explored: Human femoral neck, pig femoral neck and rat femoral head. Regardless of the type all of the structures showed the common trend that fracture toughness depends on the density of individual structures. The similar way was followed for all the cuboid trabecular bones and it was found that along with density the strength of trabecular bone depends on the types of structures.

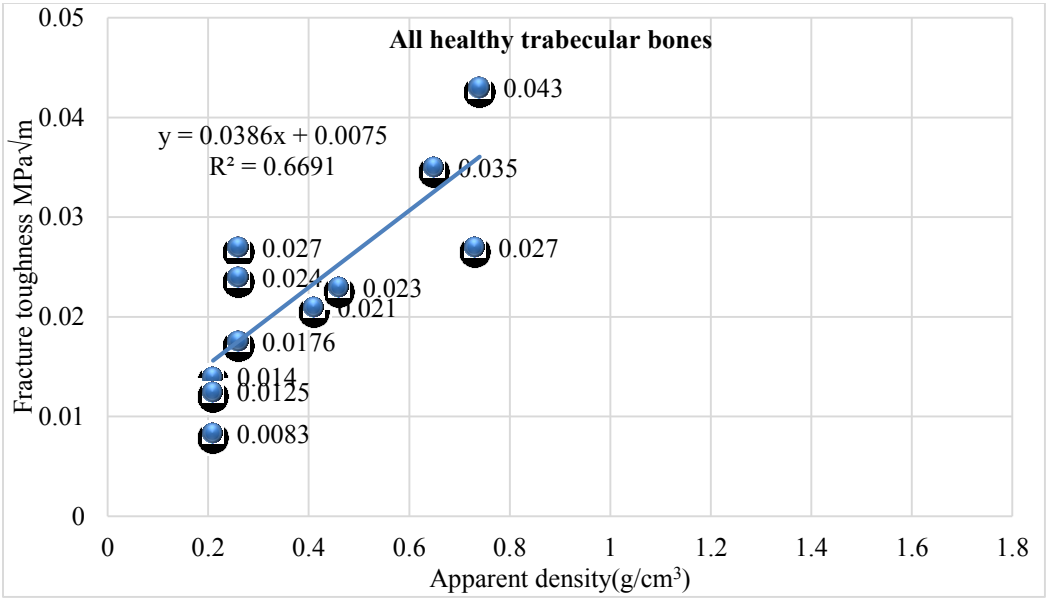

Figure 3-13 Fracture toughness vs. apparent density of all healthy trabecular bone

The universal trend line for all twelve different structures results in an equation by which the strength of trabecular bone can be approximately predicted if the value of apparent density is known.

$$Fracture\ toughness = (0.039 \times Apparent\ density)$$

Chapter 4

Effect of Density on Facture Toughness of Artificial Microstructures

Five different artificial microstructures were created with varying apparent density. Parametric models were produced and the assemblies were created with changing dimensions. The same procedure of calculating fracture toughness was followed for each assemblies. Some of the microstructures had homogeneity in two axes and were heterogeneous in another axis. All possible combinations were done to get an approximate value of fracture toughness in accordance with apparent density.

The five types of selected microstructures are true space filling and closely packed bodies. The foam bodies are created by assembling lots of unit cells. The most randomly packed cells follow a certain pattern of packing, from that point of view the assemblies of the five microstructures represent approximated foam bodies.

4.1 Hexagonal Prism

Hexagonal prism is one of the unit cells that can be packed perfectly without distortion. Three different hollow structures of the hexagonal prism unit were created. The following picture shows thinnest model with smallest apparent density.

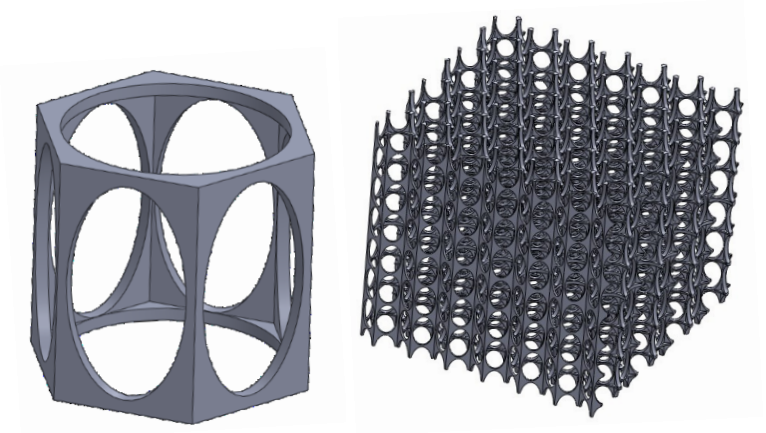

Figure 4-1 Hexagonal prism shell and its assembly

The apparent densities were varied to make the models thin, intermediate and thick. Critical stress intensity factor was calculated for all the models. The results from the table shows the value of fracture toughness increases with apparent density.

Table 4-1 Critical stress intensity factor of hexagonal prism for corresponding apparent density

Apparent Density g/cm^3	Critical Stress Intensity Factor (K_{IC}) $MPa\sqrt{m}$
0.58	0.084
0.31	0.045
0.12	0.031

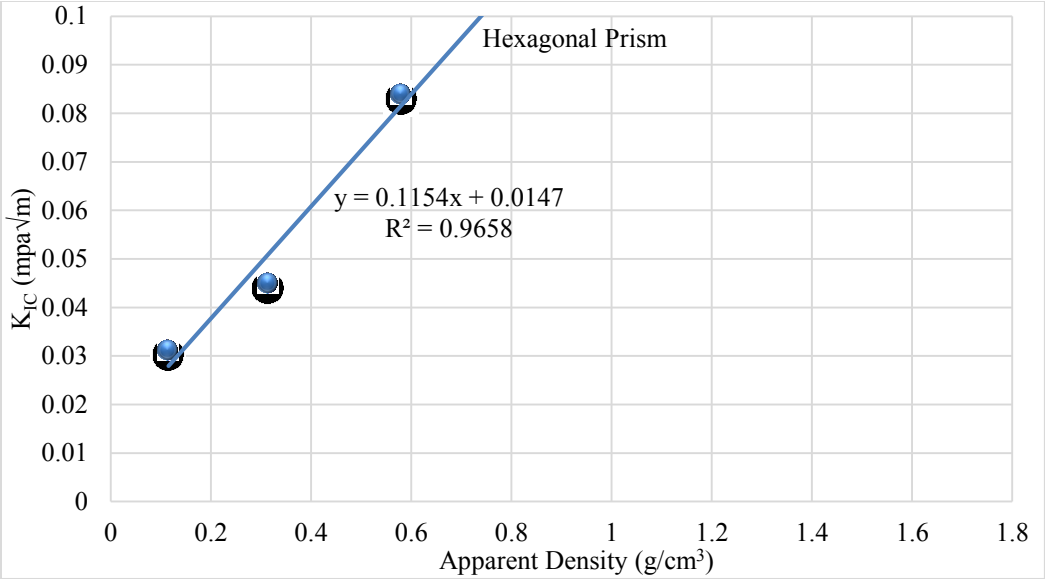

Figure 4-2 Fracture toughness vs. Apparent density of hexagonal prism

From the results it can be seen that the trend line follows the following equation:

$$Fracture\ toughness = (0.115 \times Apparent\ density) + 0.015$$

4.2 Rectangular Prism

Rectangular prism can be simply called a cuboid for this study. When assembles this microstructure is homogeneous all through its different axis. It's the simplest possible microstructure that can be packed to fill the space without any distortion.

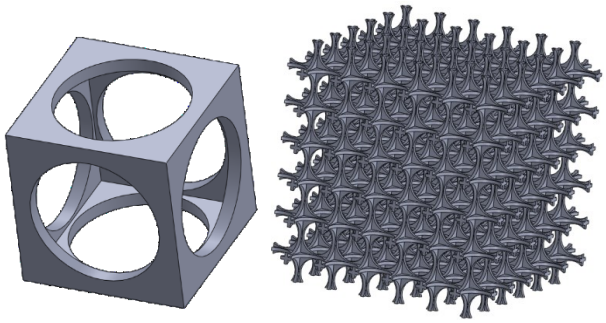

Figure 4-3 Rectangular prism shell and its assembly

The thinnest model is showed and assembly made from it. This microstructure has no axis of heterogeneity. The apparent density was varied by varying shell wall thickness.

Table 4-2 Critical stress intensity factor of rectangular prism for corresponding apparent density

Apparent Density g/cm^3	Critical Stress Intensity Factor (K_{IC}) $MPa\sqrt{m}$
0.279	0.015
0.127	0.01
0.407	0.045

They results consistently change with apparent density. The trend line expresses the linear relation between apparent density and fracture toughness.

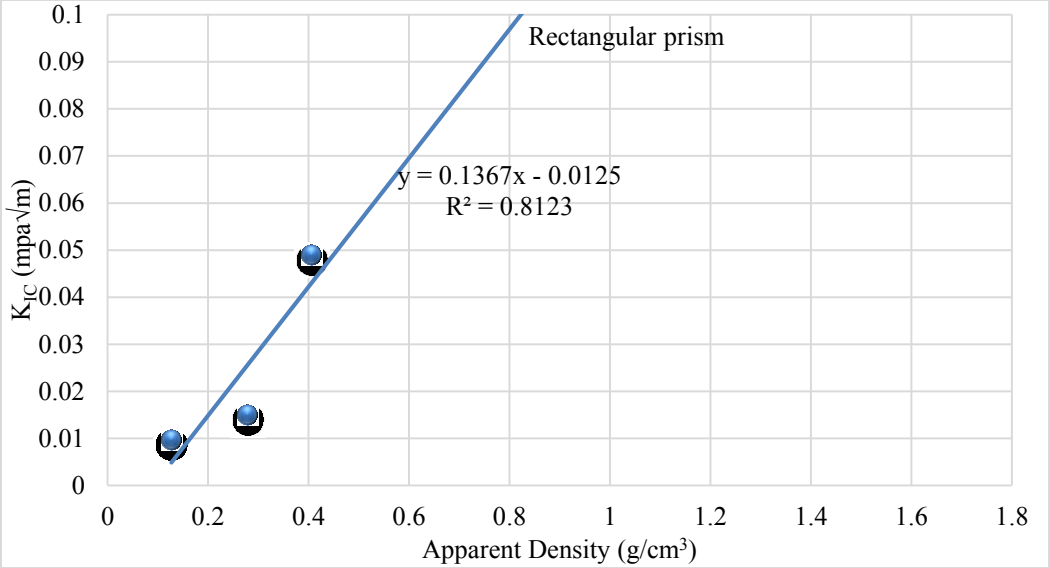

Figure 4-4 Fracture toughness vs. Apparent density of rectangular prism

From the trend line it's found that for assemblies made of rectangular prisms follows the following equation:

$$Fracture\ toughness = (0.137 \times Apparent\ density)+0.012$$

4.3 Truncated Octahedron

Truncated octahedron is one of the unit cells that can be packed in three dimensional space without leaving any vertices open. In this study truncated octahedron unit cells were used to create three assemblies with different thickness. The table shows the range of apparent density.

Table 4-3 Critical stress intensity factor of truncated octahedron for corresponding apparent density

Apparent Density g/cm^3	Critical Stress Intensity Factor (K_{IC}) MPa√m
0.54	0.013
0.70	0.02
0.34	0.01

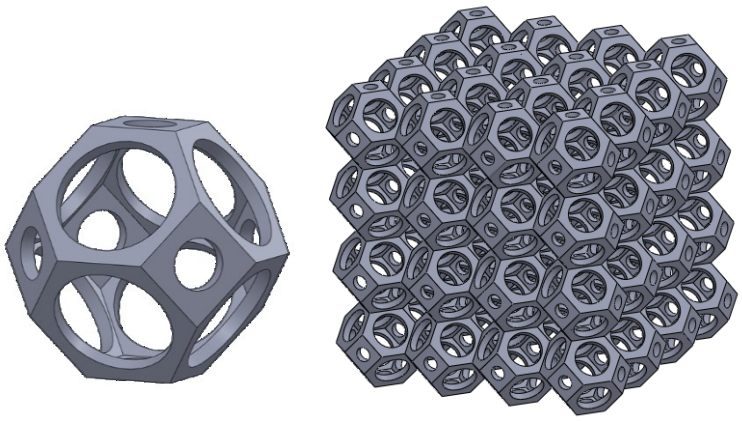

Figure 4-5 Truncated octahedron shell and its assembly

The picture shows a single unit of a truncated octahedron and an assembly. The modified crack closure method was used to find the critical stress intensity factor for these assemblies. The results showed liner increment of fracture toughness with density.

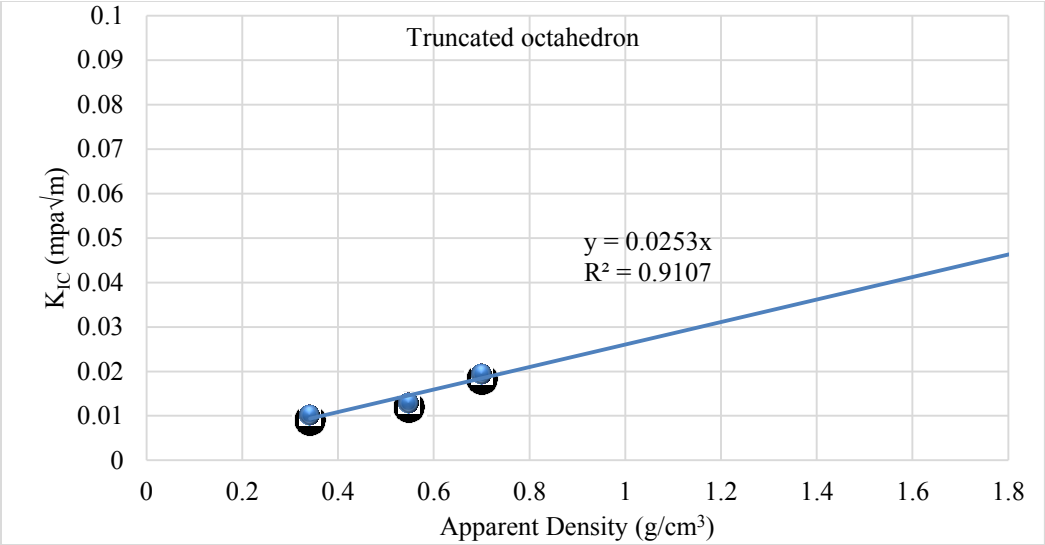

Figure 4-6 Fracture toughness vs. Apparent density of truncated octahedron

From the results the values of fracture toughness can be predicted from the trend line. The assemblies of truncated octahedron or tetrakaidehedrons shows fracture toughness properties from the equation below:

$$Fracture\ toughness = (0.025 \times Apparent\ density)$$

These results indicate that for the truncated octahedron open cell assemblies the fracture toughness doesn't drastically change with density.

4.4 Rhombic Dodecahedron

Rhombic dodecahedron is another three dimensional unit cell that can be packed in assemblies to fill the gaps in spaces without distorting or open edges. This structure is the only one which has an outer surface geometry like trabecular bone when extracted as a cuboid randomly from a large assembly.

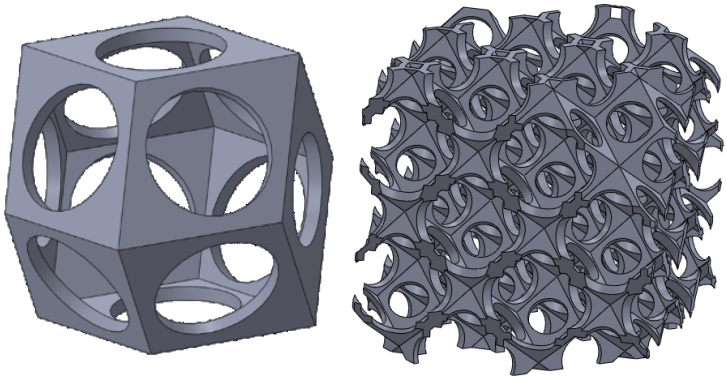

Figure 4-7 Rhombic dodecahedron shell and its assembly

In the picture a unit of rhombic dodecahedron is shown as an open cell unit. The assembly shown is the structure on which the fracture toughness study was done. Similar to other structures this unit cell was created as a parametric one and the apparent density was varied.

Table 4-4 Critical stress intensity factor of rhombic dodecahedron for corresponding apparent density

Apparent Density g/cm^3	Critical Stress Intensity Factor (K_{IC}) $MPa\sqrt{m}$
0.27	0.016
0.36	0.021
0.18	0.013

The results are show a perfect trend line from which the linear relation of fracture toughness and apparent density can be found. The following equation may be an expression of the results:

$$Fracture\ toughness = (0.05 \times Apparent\ density)$$

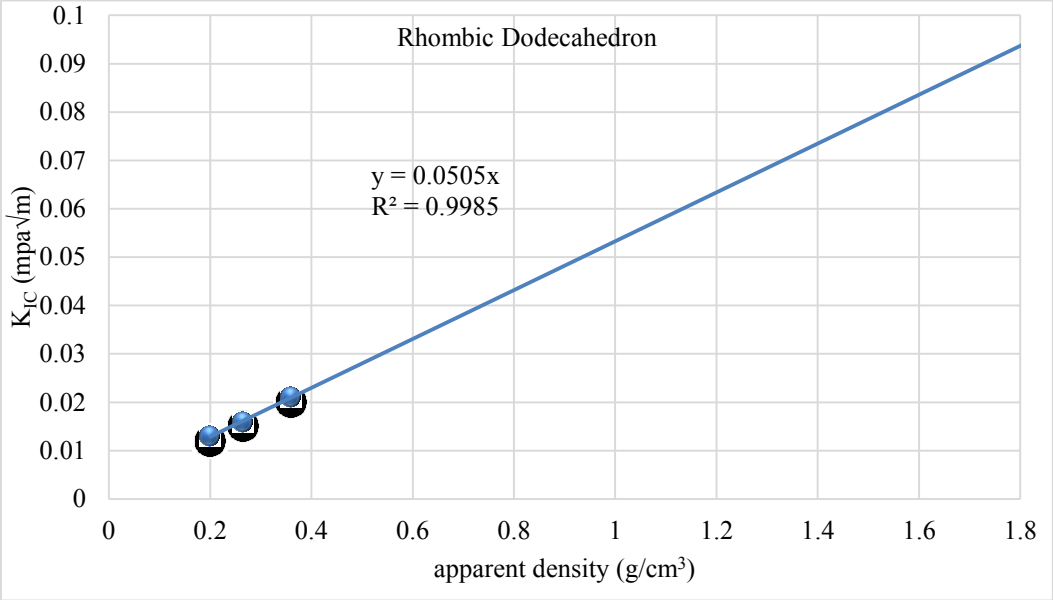

Figure 4-8 Fracture toughness vs. Apparent density of rhombic dodecahedron

4.5 Triangular Prism

Triangular prism is another unit cell which can be packed without loss to achieve perfect packing. A parametric model was used to create three different models with three different densities. The table shows the values of density and corresponding critical stress intensity factor.

Table 4-5 Critical stress intensity factor of triangular prism for corresponding apparent density

Apparent Density g/cm^3	Critical Stress Intensity Factor (K_{IC}) $MPa\sqrt{m}$
0.459	0.073
0.508	0.089
0.165	0.0474

In the picture a unit open foam cell created from the basic triangular prism is shown and the assembly was created from the unit cell. Three assemblies with densities were created like the other structures.

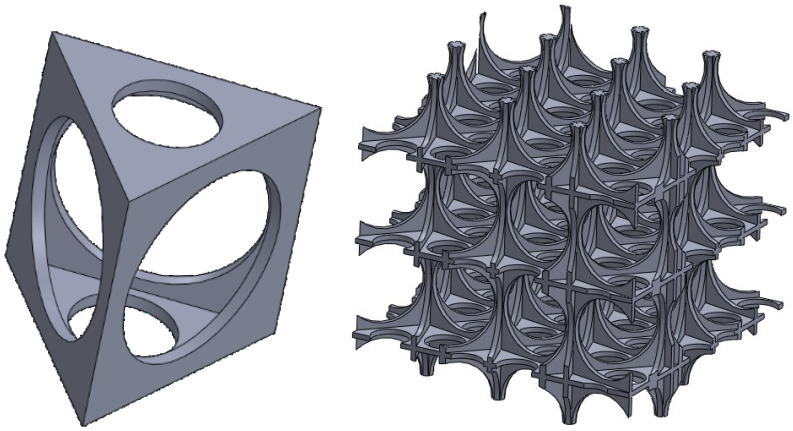

Figure 4-9 Triangular prism shell and its assembly

The fracture toughness study was done in the same way as the previous structures using modified crack closure method. The results shows an approximated linear increment of the fracture toughness values with the increasing apparent density.

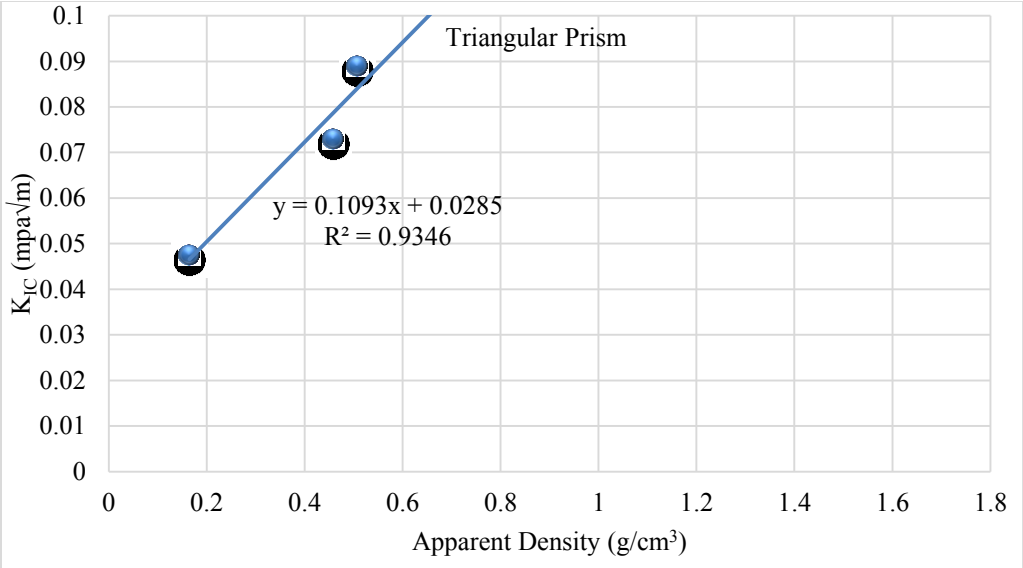

Figure 4-10 Fracture toughness vs. Apparent density of triangular prism

The following equation can be assigned to this result set for triangular prism assemblies:

$$Fracture\ toughness = (0.109 \times Apparent\ density) + 0.029$$

4.6 Comparing Fracture Toughness of Trabecular Bone with Artificial Microstructures

The fracture toughness or critical stress intensity factor values were collected from all the simulations in this chapter and the previous chapter. For each microstructure an individual linear equation was found from the line curves. These equations are the fracture toughness values in MPa√m as a function of apparent density in g/cm^3.

Table 4-6 Summery of equations representing fracture toughness as a function of apparent density

Structure type	Relation between Fracture Toughness (FT) and Apparent Density (AD)	Average Fracture Toughness (Apparent density=1 g/cm^3) MPa√m
Trabecular bone	*FT=0.039AD*	0.039*
Hexagonal prism	*FT=0.115AD+0.015*	0.13
Rectangular prism	*FT=0.137AD+0.012*	0.149
Rhombic dodecahedron	*FT=0.05AD*	0.05*
Triangular prism	*FT=0.109AD+0.029*	0.14
Truncated octahedron	*FT=0.025AD*	0.025

In each case the apparent density was assumed 1 g/cm^3 and the equations delivered the values of fracture toughness in a common standard for all the structures. By observing the results it was found that the fracture toughness values of rhombic dodecahedron* was close to the fracture toughness value of trabecular bone*.

Chapter 5

Comparative Structural Stiffness and Effect Of Anisotropy between Micro CT Scan Image Based Real Bone Structure and Approximated Microstructure

Elastic modulus is the measure of stiffness of any structure. By analyzing the elastic modulus of the structures an overall comparative study can be done with respect to their ability to withstand stress. In this comparative study of stiffness a certain technique was followed to estimate the isotropic elastic modulus of the individual structures.

For the trabecular bone study the structures with difference in transverse and longitudinal axis were taken into consideration. Elastic modulus were estimated for different planes. The load was applied along different axis and the plane on other two axis was fixed. The applied load was displacement and the total mechanical strain was calculated from the corresponding displacement for all structures. The force was calculated at the fixed surface at the bottom plane. Total force after displacement was summed up for each fixed surface. The stress was calculated by dividing the force with area, the area was defined by the complete bounding box of the fixed surface including the occupied area and the void.

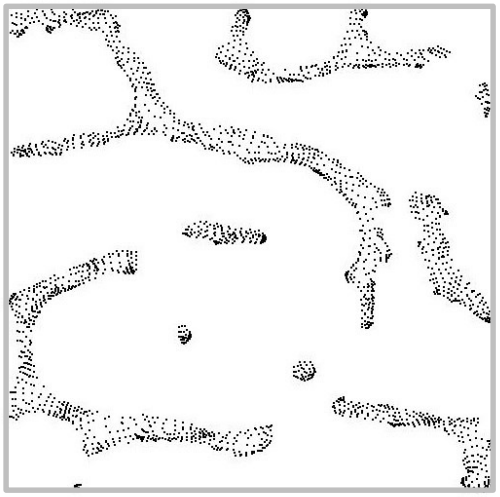

Figure 5-1 Cross section of trabecular bone showing the solid part and the void part

The picture shows one example of the trabecular bone fixed surface, the bounding box is the area that was used to calculate the stress from the force. Each dots on the surface represent a node, the values of all nodes were summed and the total stress on that surface was calculated.

The same procedure was followed for all the trabecular bone collected and for all the artificial microstructures. The following chapters show the results and comparisons.

5.1 Human Bone

Elastic modulus of the human femoral neck trabecular bone was estimated for the three different trabecular bone models. Stress and strain values were collected from the force and displacement values accordingly. Linear stress-strain curve was plotted for all the three models.

Table 5-1 List of stress, displacement and force results for different human trabecular bones

Apparent Density g/cm^3	Loading Axis	Strain %	Stress MPa	Avg Stress MPa	Displacement mm	Force N
0.21	x-transverse	3.75	0.85	0.64	0.15	13.701
	y-transverse		0.33			5.3318
	z-longitudinal		0.75			12.458
0.26	x-transverse		1.63	1.14		26.001
	y-transverse		0.41			6.5214
	z-longitudinal		1.38			22.059
0.59	x-transverse		6.94	4.78		111.11
	y-transverse		2.88			46.087
	z-longitudinal		4.51			72.576

The table shows the applied displacement load and corresponding force, strain and stress values. For all the three models the same load was applied which was 0.15mm. The post processing of the results involved estimating the stress values from the summation of forces.

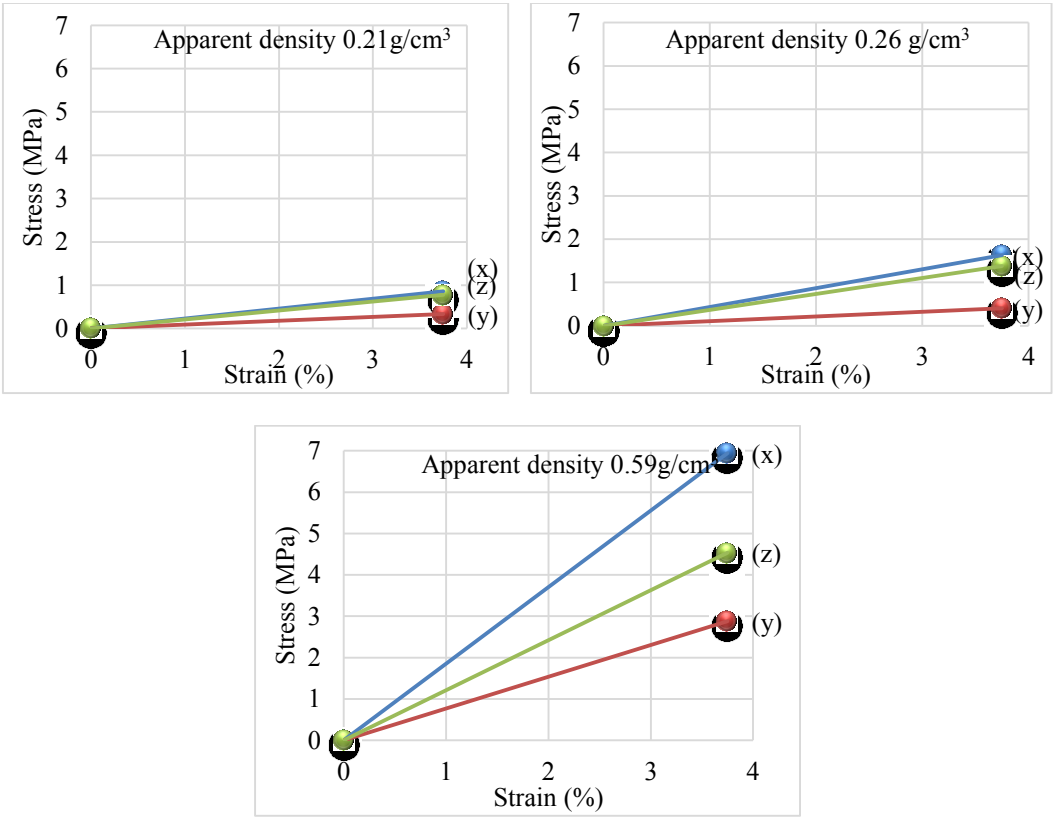

Figure 5-2 Stress-strain line curve of thin, intermediate and thick human trabecular bone

The stress-strain linear plots show the maximum stress bearing capacity increases with density. The three different models were subjected to the same displacement load and the results indicate that the stress values increase drastically with density linearly.

Table 5-2 Elastic modulus and apparent density of human trabecular bone

Apparent Density g/cm^3	Elastic Modulus GPa
0.21	0.017
0.26	0.0304
0.59	0.123

The table shows the corresponding elastic modulus of the trabecular structures with respect to the apparent density.

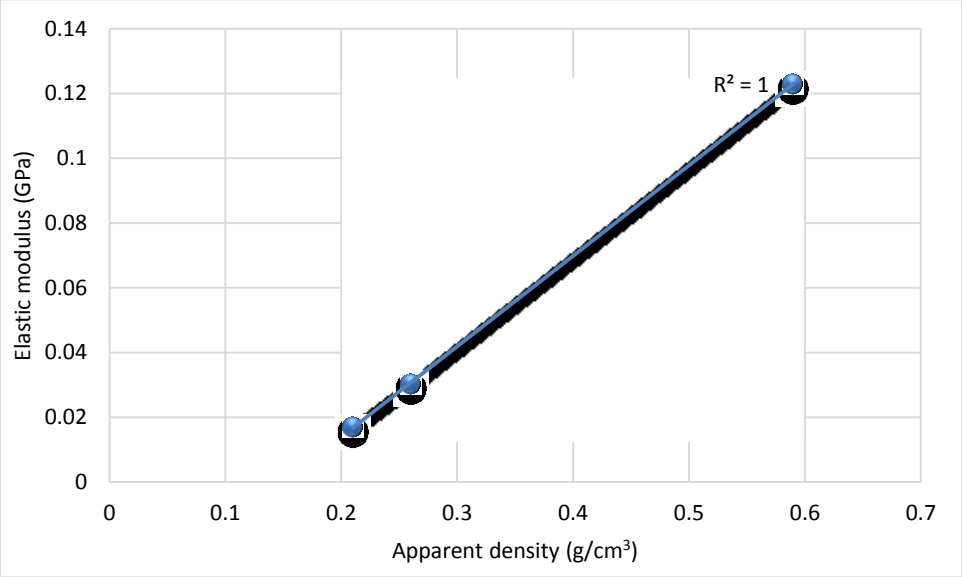

Figure 5-3 Elastic modulus vs. apparent density of human trabecular bone

5.2 Pig Bone

Three trabecular bones were selected from the collected pig femoral neck trabecular bones depending on apparent densities. The same procedure was used for all the three trabecular bone to find the stress for the corresponding applied displacement. The displacement load was applied along all three axis and the stiffness property was estimated.

Table 5-3 List of stress, displacement and force results for different pig trabecular bones

Apparent Density g/cm^3	Loading axis	Strain %	Stress (MPa)	Avg Stress MPa	Displacement (mm)	Force (N)
0.74	z	4	10.51	17.37	0.1	103
	x		21.72			58.21
	y		19.89			82.62
0.66	z		16.52	13.02		65.62
	x		9.33			135.73
	y		13.22			124.32
0.42	z		7.92	5.99		49.51
	x		4.69			29.33
	y		5.38			33.64

The table shows stress for 4% strain and the force values for 0.1 displacement. The results were used to plot the stress- strain points. For the three trabecular models the stress-strain was plotted and the difference in the stress bearing capacity is showed in the graphs.

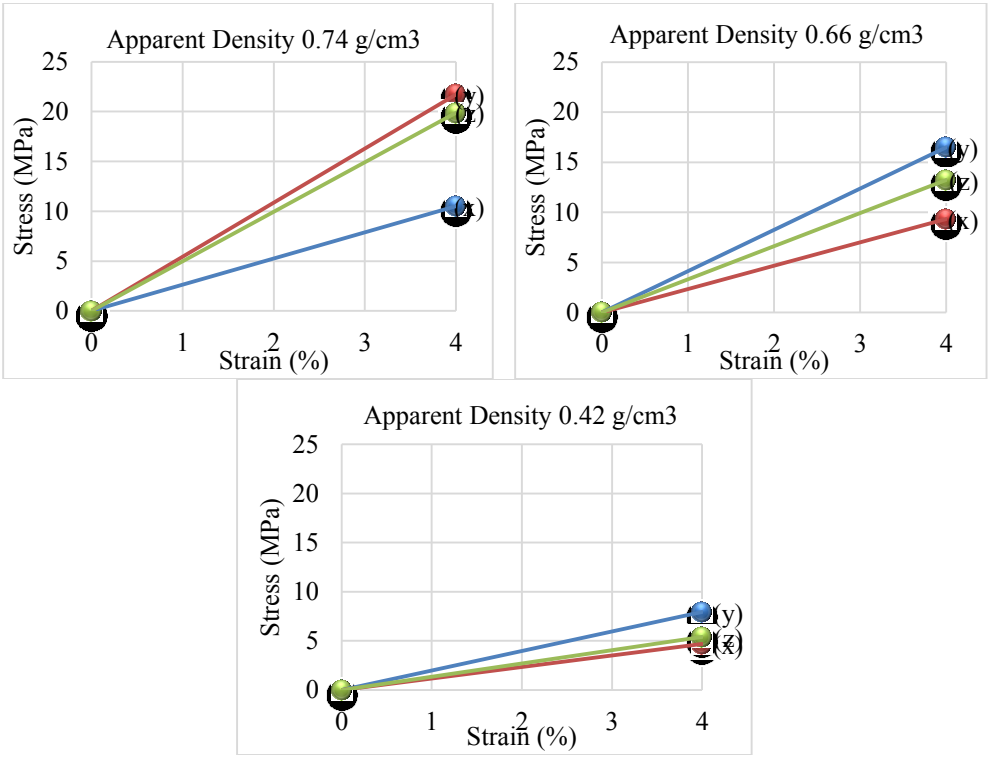

Figure 5-4 Stress-strain line curve of thin, intermediate and thick pig trabecular bone

The graphs show the model with the highest apparent density has the maximum stress, hence the maximum elastic modulus is found from the thickest trabecular structure.

Table 5-4 Elastic modulus and apparent density of pig trabecular bone

Apparent Density g/cm^3	Elastic Modulus GPa
0.74	0.43
0.66	0.32
0.42	0.15

The average stress was calculated for all the structures and the corresponding elastic modulus was found. The R squared value for the points is nearly perfect which explains the case.

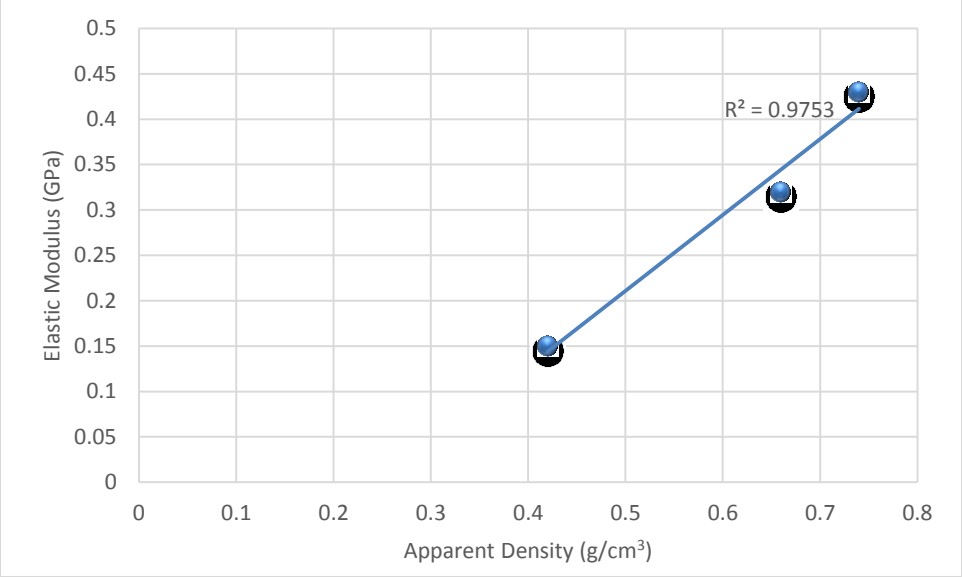

Figure 5-5 Elastic modulus vs apparent density of pig trabecular bone

5.3 Rat Bone

One of the femoral head trabecular bones was selected for analysis. Among all the collected four the others were not selected for inappropriate dimensions. The similar procedure was followed for estimating elastic modulus for the rat bone. Load was applied on different axis of the trabecular bone and the output stress was collected against applied boundary condition

Table 5-5 List of stress, displacement and force results for rat trabecular bones

Apparent Density g/cm^3	Loading axis	Strain %	Stress (MPa)	Average stress (MPa)	Displacement (mm)	Force (N)
1.01	x	1.6	9.019	11.67	0.0119	3.2468
	y		18.61		0.0108	6.6988
	z		7.396		0.0115	2.6625

The average stress was calculated in the table from the force results and the elastic modulus was calculated which was 0.73 GPa.

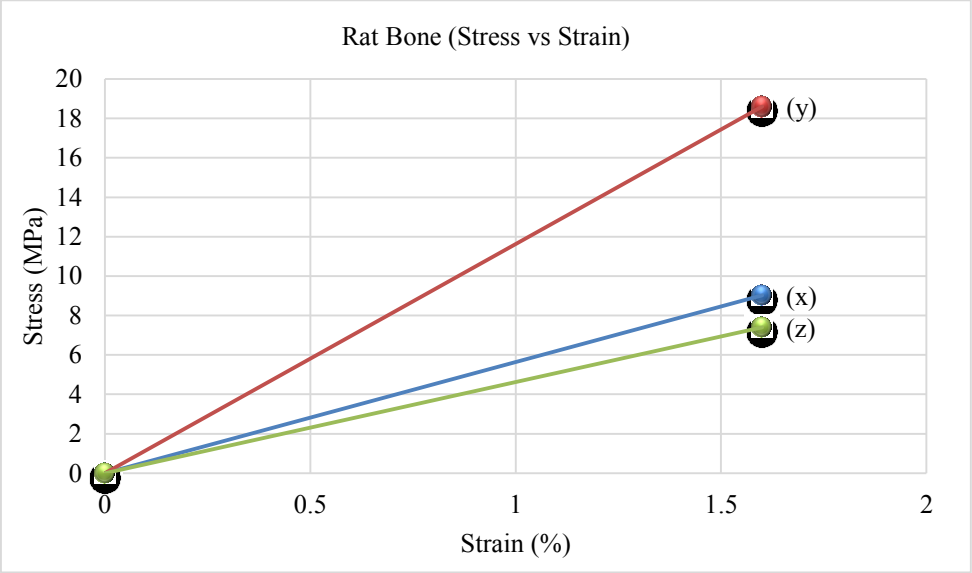

Figure 5-6 Stress-strain line curve of rat trabecular bone

5.5 Comparison of All Trabecular Bones

All the trabecular bones' elastic modulus were put all together in a table and a statistical graph was obtained. The results show that the value of elastic modulus increases drastically with apparent density.

Table 5-6 4 Elastic modulus and apparent density of human trabecular bone

Apparent Density g/cm^3	Elastic Modulus GPa
0.21	.023
	.009
	.02
0.26	.043
	0.11
	.04
0.42	0.19
	0.11
	0.13
0.59	0.18
	.08
	0.12
0.66	0.41
	0.23
	0.33
0.74	0.26
	0.54
	0.49
1.01	0.56
	1.16
	0.46

The R squared value for the exponential trend line is 0.83 which means the points fit the exponential equation better than the linear trend line (R^2=0.645). The exponential equation that can relate the relation of elastic modulus and apparent density is:

$$Elastic\ Modulus = 0.019e^{(0.18 \times Apparent\ Density)}$$

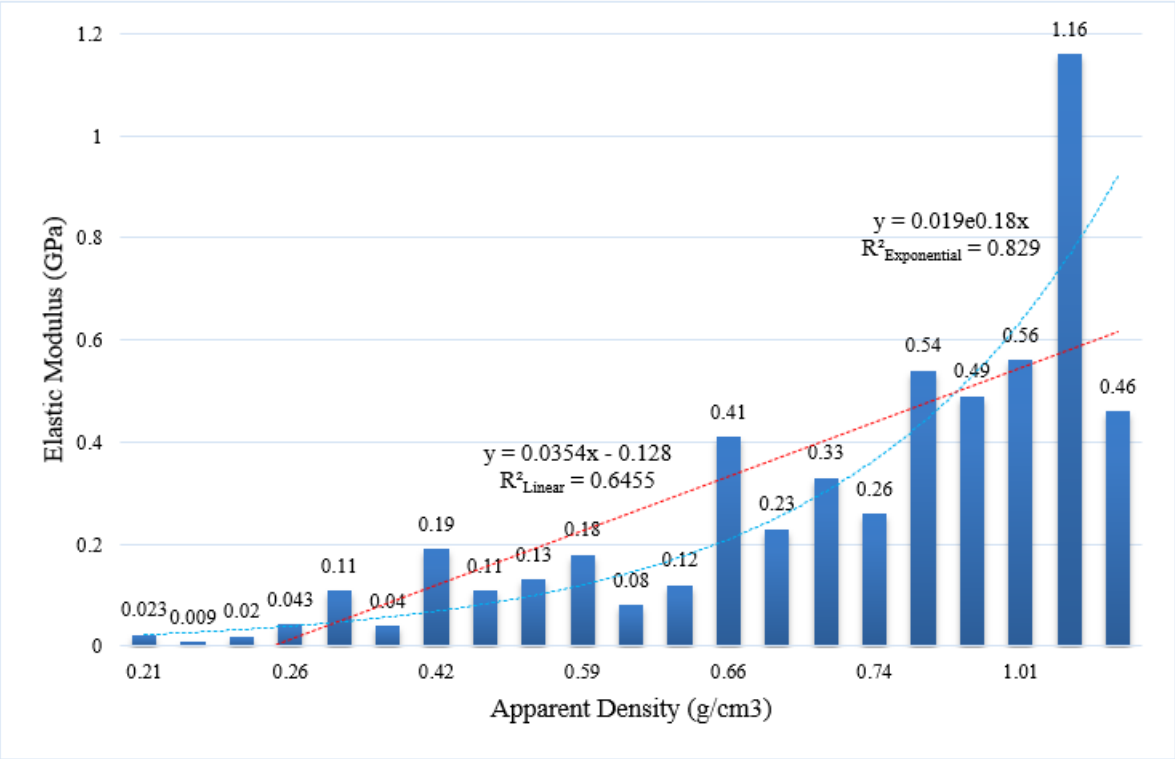

Figure 5-7 Elastic modulus vs. apparent density for all trabecular bones

Chapter 6

Effect of Density on Elastic Modulus of Artificial Microstructures

6.1 Hexagonal Prism

Hexagonal prism has a longitudinal axis and two transverse axis. The same procedure was applied for hexagonal prism for estimating elastic modulus of the assemblies including the void part. Displacement was applied on different axis and the plane on the other two axis was fixed. It was found that the two transverse axis have exact same results. The longitudinal axes was stronger.

Table 6-1 List of stress, displacement and force results for different hexagonal prism assemblies

Apparent Density g/cm^3	Loading Axis	Strain %	Stress MPa	Avg Stress MPa	Displacement mm	Force N
0.12	x-Transverse	3.3	0.33	3.45	0.1	2.9717
	y-Longitudinal		6.58			59.205
0.31	x-Transverse		1.89	12.5		16.996
	y-Longitudinal		23.1			207.52
0.58	x-Transverse		4.94	29.1		44.418
	y-Longitudinal		53.2			479.2

The three different assemblies of hexagonal prism were analyzed. Each assembly with low to high apparent density shows individually different output results. The thin structure has the lowest stress bearing capability, the intermediate was higher and the thick one was the strongest.

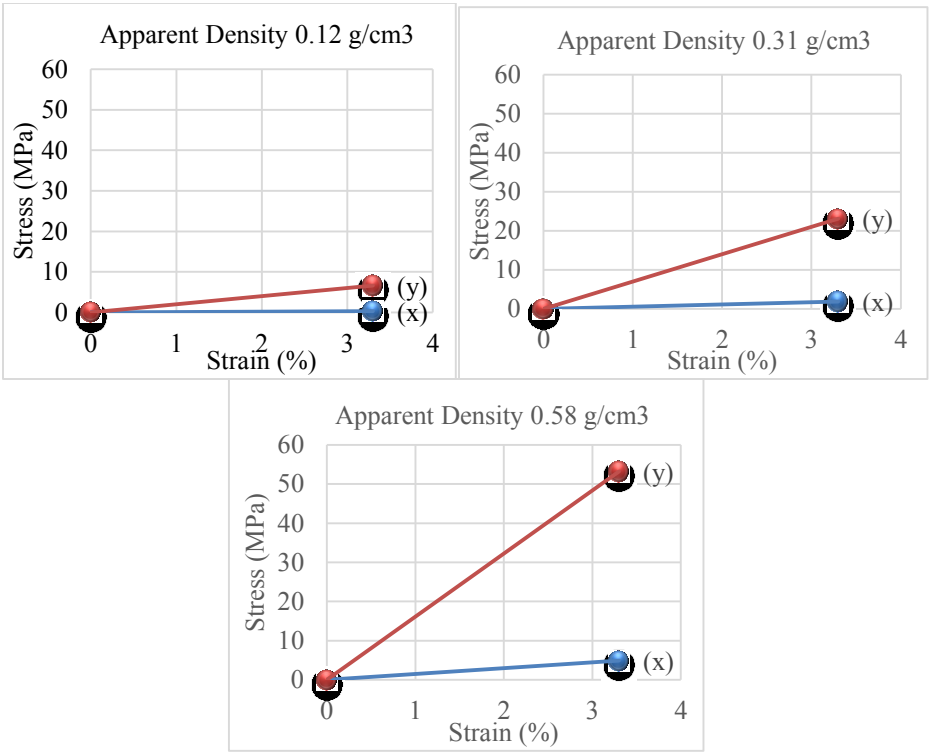

Figure 6-1 Stress-strain line curve for hexagonal prism assemblies

All the results were plotted in graphs with the same axis bounding values. The difference is visible from the graphs. All the assemblies were cuboids of 3mm length. Stress values were calculated from the forces found.

Table 6-2 Elastic modulus for corresponding apparent density of hexagonal prism

Loading Axis	Apparent Density g/cm^3	Elastic Modulus GPa
Transverse	0.12	0.01
	0.31	0.05
	0.58	0.15
Longitudinal	0.12	0.2
	0.31	0.7
	0.58	1.61

All the elastic modulus results were separated into two groups: transverse and longitudinal. The calculated elastic modulus values were plotted against their apparent densities. From the graph it can be predicted that the elastic modulus of the structures loaded along the longitudinal axis is much higher than the transverse axis.

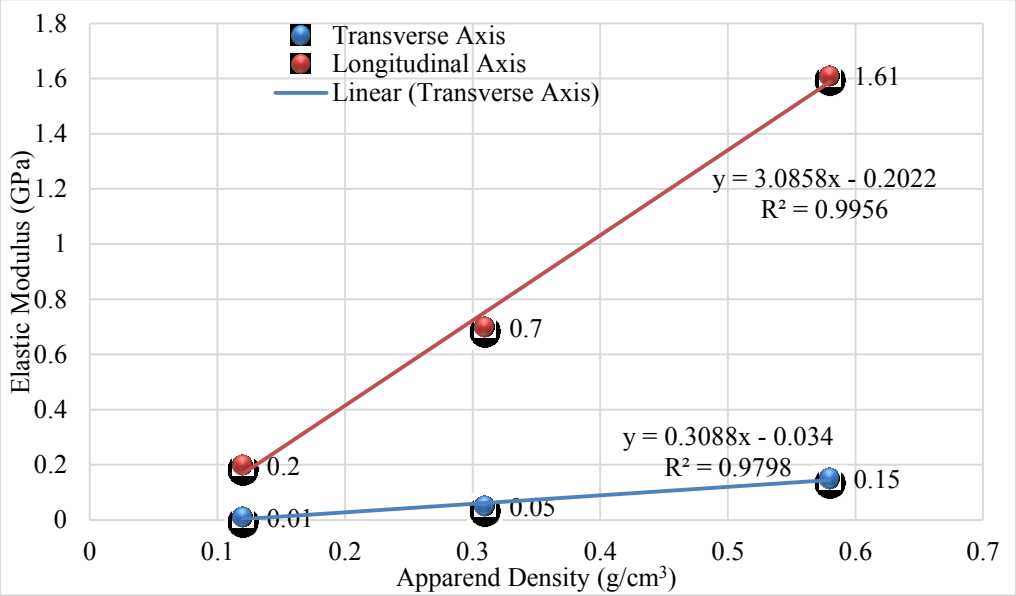

Figure 6-2 Comparison of elastic modulus between transverse and longitudinal axis of hexagonal prism

For hexagonal prism assemblies two equations can be drawn for the longitudinal axis and the transverse axis.

$$E(\text{Transverse}) = 0.3088\ (\text{Apparent Density}) - 0.034$$
$$E\ (\text{Longitudinal}) = 3.0858\ (\text{Apparent Density}) - 0.202$$

6.2 Rectangular Prism

In this study rectangular prism was converted into cubic prism with equal length. The assemblies found from this unit cell had no axis of inhomogeneity. Hence the results from all axis were identical.

Table 6-3 List of stress, displacement and force results for different rectangular prism assemblies

Apparent Density g/cm^3	Strain %	Stress MPa	Displacement mm	Force N
0.12		1.7		15.279
0.28	3.3	3.21	0.1	28.914
0.41		4.85		43.64

For three different assemblies with three different apparent densities were subjected to 3.3% strain on random planes. One face was fixed and the other faces were loaded with displacement boundary condition.

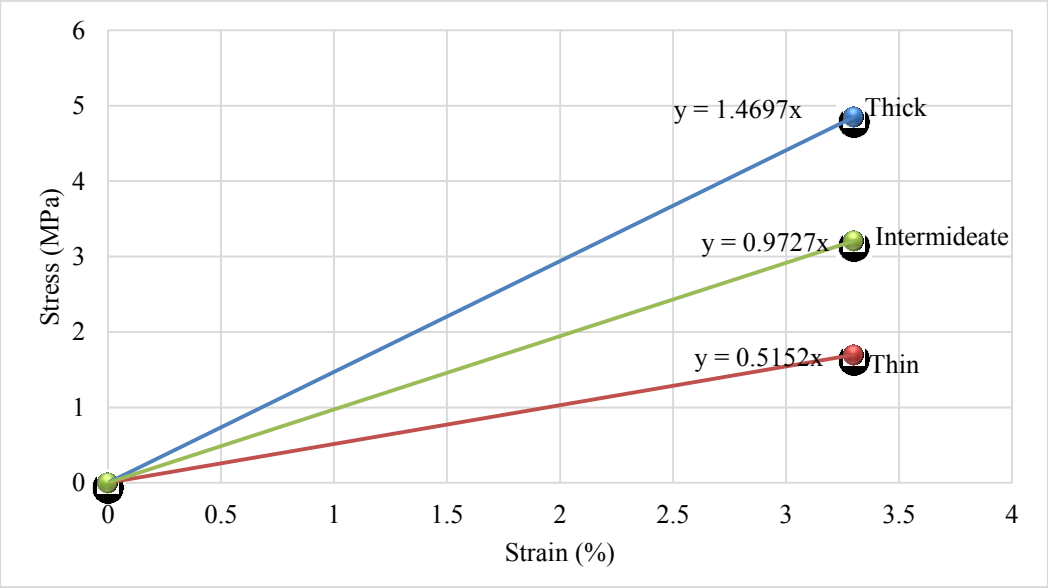

Figure 6-3 Stress-strain line curve for rectangular prism assemblies

It can be found from the graph that the thickest structure has the highest elastic modulus. The slope of the lines are the elastic modulus of the corresponding structures. The elastic modulus of the thick, intermediate and thin structure is accordingly: 0.15 GPa, 0.1 GPa and 0.05GPa.

6.3 Rhombic Dodecahedron

Rhombic dodecahedron shows inhomogeneity along all the axis. A cuboid was subtracted from all the assemblies of different densities and the previous procedure was applied to all of them. One face was fixed and the opposite face was loaded with displacement boundary condition.

Table 6-4 List of stress, displacement and force results for different rhombic dodecahedron assemblies

Apparent Density g/cm^3	Loading Axis	Strain %	Stress MPa	Avg Stress MPa	Displacement mm	Force N
0.18	x	3.3	0.71	0.71	0.1	6.41
	y		0.81			7.21
	z		0.62			8.16
0.27	x		0.92	0.98		5.62
	y		1.11			9.98
	z		0.91			8.16
0.36	x		1.65	1.85		14.83
	y		2.4			21.56
	z		1.51			13.56

All the different axis showed different strengths without following any pattern. The corresponding stress was estimated including the void space in calculation. All the results were plotted it was found that the elastic modulus along all the axis gets stronger with increasing density of solid.

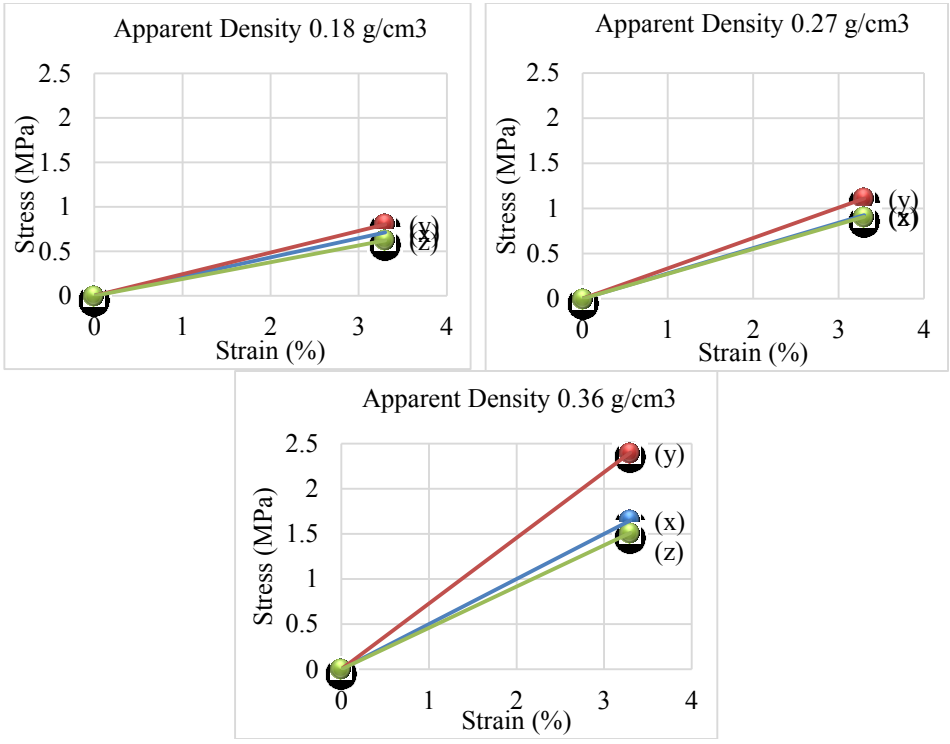

Figure 6-4 Stress-strain line curve for rhombic dodecahedron assemblies

All the results were grouped in the groups according to the apparent density. Elastic modulus was estimated for all the obtained results along different axis and planes. The following table shows the Elastic modulus and corresponding apparent density.

Table 6-5 Elastic modulus for corresponding apparent density of rhombic dodecahedron

Apparent Density g/cm^3	Elastic Modulus GPa
0.18	0.021
	0.024
	0.019
0.27	0.028
	0.034
	0.027
0.36	0.05
	0.072
	0.045

The elastic modulus values were plotted against the apparent density and two different trend line were obtained. The exponential trend line shows more accurate R squared value then the linear tend line. So in this case the exponential line was chosen to be acceptable.

From the results and trend lines it can be concluded that the elastic modulus of rhombic dodecahedron assemblies follows the following rule:

$$Elastic\ Modulus = 0.0163e^{0.1374\ (Apparent\ density)}$$

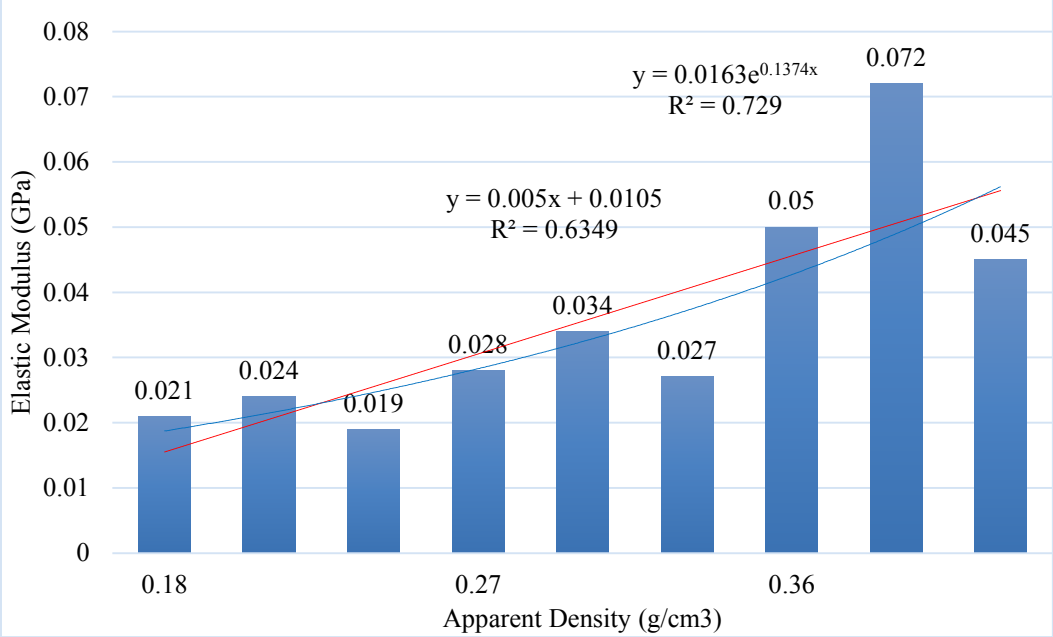

Figure 6-5 Comparison of elastic modulus against apparent density of rhombic dodecahedron

6.4 Triangular Prism

Triangular prism assemblies has inhomogeneity along its axis. It has a longitudinal axis and two transverse axis. The two transverse axis shows almost identical results. Hence in this study one transverse axis and the longitudinal axis were taken into account.

Table 6-6 List of stress, displacement and force results for different triangular prism assemblies

Apparent Density g/cm^3	Loading Axis	Strain %	Stress MPa	Avg Stress MPa	Displacement mm	Force N
0.16	y-Longitudinal	3.3	5.49	3.72	0.1	49.4
	x-Transverse		1.96			17.6
0.46	y-Longitudinal		23.1	14.81		209.8
	x-Transverse		6.53			58.8
0.51	y-Longitudinal		24.7	16.5		222.2
	x-Transverse		8.28			74.5

Y axis is the longitudinal axis and the other two axis was transverse. For each model with individual apparent density 3.3% strain was applied. In the table the output results are shown. Similar to the previous calculations the stress values were estimated from the forces found.

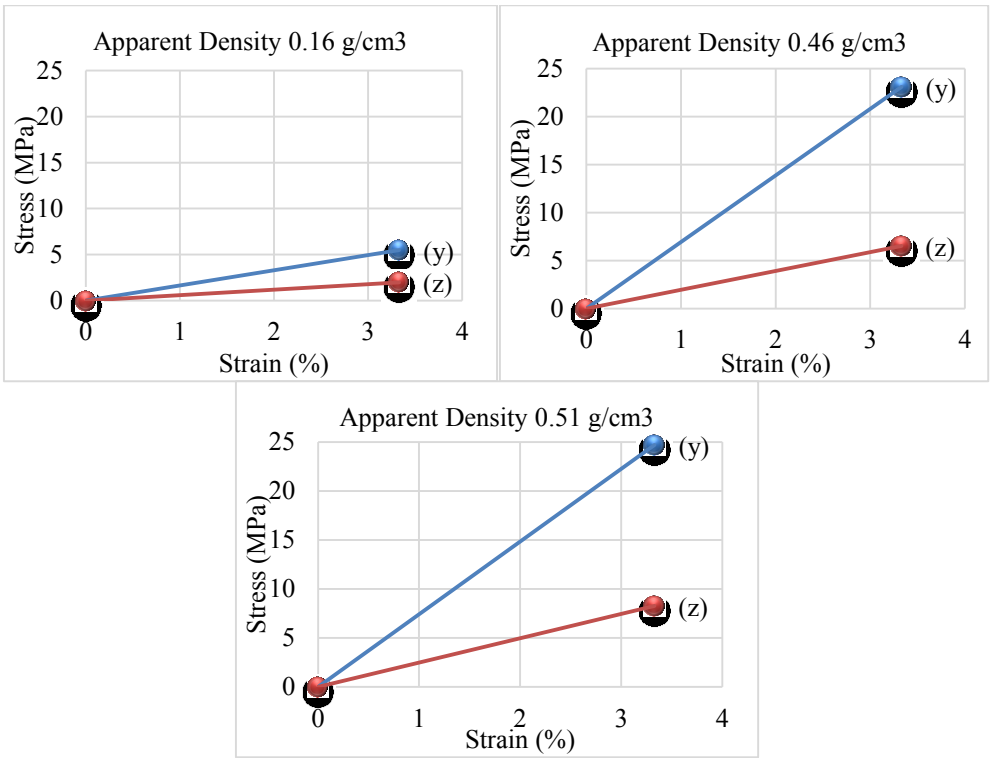

Figure 6-6 Stress-strain line curve for triangular prism assemblies

The stress-strain curve was plotted for all three models and the corresponding elastic modulus was found from the slopes. In the following table the elastic modulus was separated in two groups for transverse axis and longitudinal axis.

Table 6-7 Elastic modulus for corresponding apparent density of triangular prism

Loading Axis	Apparent Density g/cm^3	Elastic Modulus GPa
Transverse	0.16	0.06
	0.46	0.2
	0.51	0.25
Longitudinal	0.16	0.17
	0.46	0.7
	0.51	0.75

The elastic modulus values were plotted from the table against apparent density and two trend line was obtained for transverse axis and longitudinal axis. From the slopes it can be concluded as:

$$E(Transverse) = 0.516\ (Apparent\ Density) - 0.024$$

$$E\ (Longitudinal) = 1.69\ (Apparent\ Density) - 0.099$$

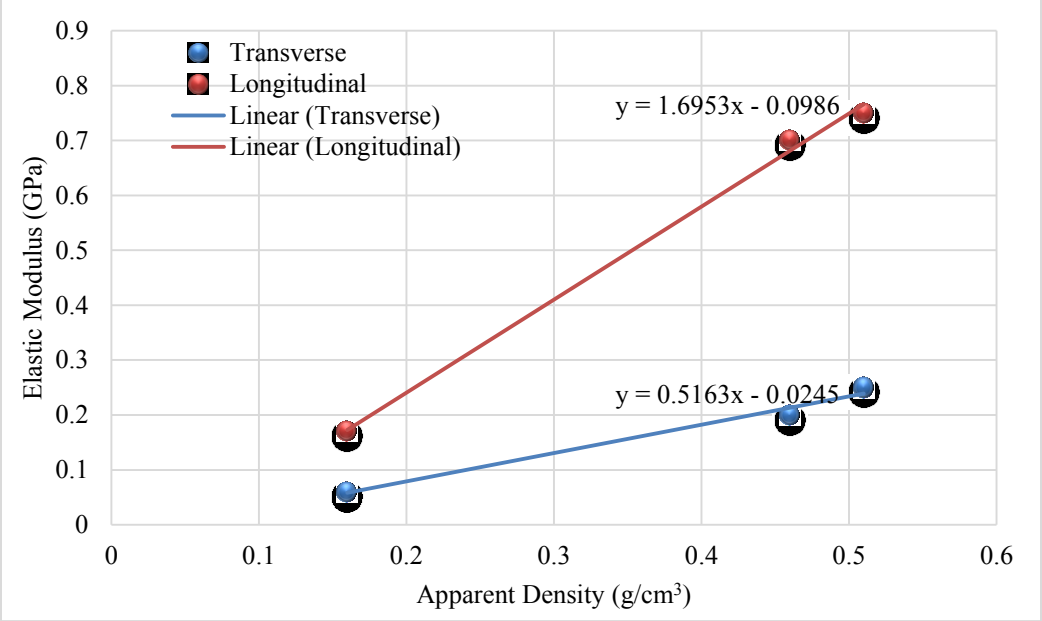

Figure 6-7 Comparison of elastic modulus between transverse and longitudinal axis of triangular prism

6.5 Truncated Octahedron

Truncated octahedron has homogeneity in all three axis, so for all the assemblies only one axis was selected as the loading axis. In analysis of one model all three axis showed similar results when loaded with similar strain.

Table 6-8 List of stress, displacement and force results for different truncated octahedron assemblies

Apparent Density g/cm^3	Strain %	Stress MPa	Displacement mm	Force N
0.34	3.3	0.5	0.1	4.298
0.54		0.75		6.771
0.70		0.47		4.261

The corresponding stress was estimated for the force found from the simulations and plotted in a graph against applied strain which is 3.3% of the initial length. Three lines can be found from the points plotted, slope of which represents the elastic modulus of the models. For the thick, intermediate and the thin model was estimated to have elastic modulus accordingly: 0.023 GPa, 0.015 GPa and 0.014 GPa.

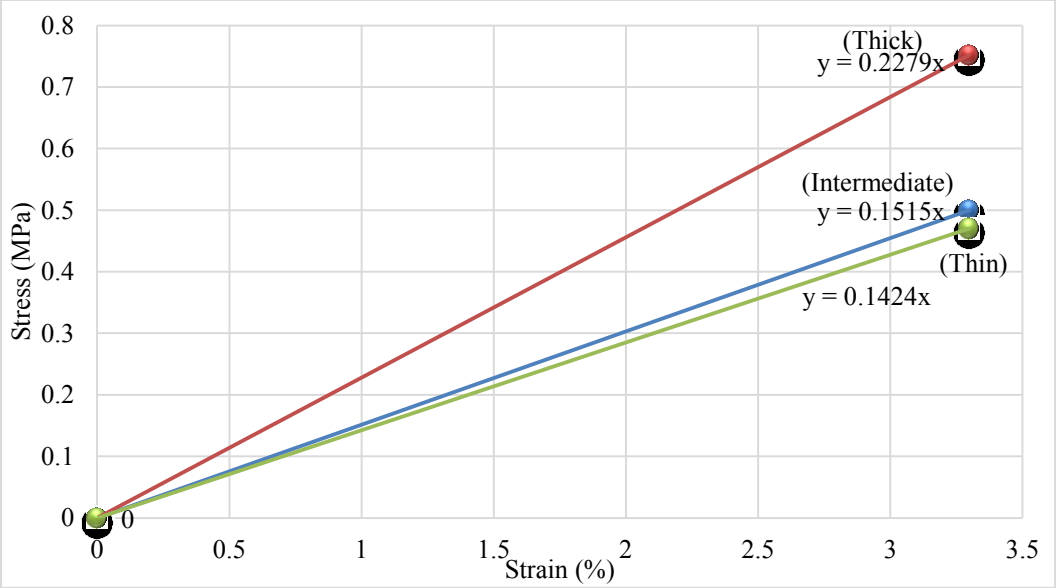

Figure 6-8 Stress-strain line curve for truncated octahedron assemblies

6.6 Comparing Elastic Modulus of Trabecular Bone with Artificial Microstructures

All the results were summarized in a table from the previous chapters of estimating elastic modulus. For all the models the Elastic modulus equations were converted to expect output values in GPa. Apparent density was g/cm^3 for all the models. The relations between these two properties were established by multiplying constants. In table 6-9 all the equations were noted and the average elastic modulus was calculated by assuming apparent density was 1 g/cm^3 for all the cases to obtains an equal comparable standard.

Table 6-9 Summery of equations between elastic modulus and apparent density for all microstructures

Structure type	Relation between Elastic modulus (E) and Apparent Density (AD)	Average Elastic modulus (Apparent density=1 g/cm^3) GPa
Trabecular bone	$E=0.019e^{0.18AD}$	0.022*
Hexagonal prism	$E_{(Transverse)} = 0.31AD - 0.034$, $E_{(Longitudinal)} = 3.0858AD - 0.202$	1.58
Rectangular prism	$E_{Thick}=0.15AD$, $E_{Intermediate}=0.1AD$, $E_{Thin}=.05AD$	0.1
Rhombic dodecahedron	$E=0.016e^{0.14AD}$	0.018*
Triangular prism	$E_{(Transverse)} =0.16AD-0.024$, $E_{(Longitudinal)} = 1.69AD-0.1$	0.863
Truncated octahedron	$E_{Thick}=0.023AD$, $E_{Intermediate}=0.015AD$, $E_{Thin}=.014AD$	0.017

The average apparent densities were calculated and it was found that the average elastic modulus of rhombic dodecahedron* and trabecular bone* are closest among all the other micro structures. From the elastic modulus study it can be concluded that among the five possible three dimensional artificial microstructures rhombic dodecahedron neatly represents almost equivalent elastic properties of trabecular bone.

Chapter 7

Fabrication of Bone Structure with Pure Epoxy/Nano Si-C Phased Epoxy Polymer

The use of biomaterials in the form of implants (bone plates, joint replacements, ligaments, dental implants etc.) dates far back into ancient civilizations. The biomaterials should have both biocompatibility (that is it should be able to perform with the appropriate host response in a specific application) and structural compatibility (that is the optimal adaptation to the mechanical behavior of host tissue). Structural compatibility refers to mechanical properties such as elastic modulus, stiffness and optimal load transmission at the implant/tissue interface.

While various materials like metals, ceramics, polymers, composites and combinations of all these can be used as biomaterials, metals and ceramics are extensively used in biomedical applications and the use of polymer composites is being explored recently. Polymers are widely used in various applications because of their availability in wide variety of compositions, properties and forms (solids, fibers, fabrics, films, and gels) and can be fabricated readily into complex shapes and structures. But since they tend to be too flexible and weak, their use has been limited to soft tissues only.

Metals have high strength, ductility and wear resistance but they are not so biocompatible due to high density, corrosion, high stiffness compared to tissues and also release of metal ions which may cause allergic reactions to the tissues. In this regard, ceramics are good since they have corrosion resistance and high compression resistance. But they are brittle and have low fracture strength and resilience. Polymer composite materials provide an alternate choice to overcome the shortcomings of homogeneous materials (Ramakrishna and Mayer).

One of the major problems in orthopedic surgery is the mismatch of stiffness between the bone and metallic or ceramic implants. In the load sharing between the bone and implant, the amount

of stress carried by each of them is directly related to their stiffness. Thus, bone is insufficiently loaded compared to the implant, and this phenomenon is called 'stress-shielding' or stress protection. The stress-shielding affects the bone remodeling and healing process leading to increased bone porosity (also known as bone atrophy). So, material with lower elastic modulus and high strength is needed. Polymers alone have low elastic modulus but they lack strength. But when reinforced the strength can be significantly improved to match the required property of the implant. Thus, the polymer composites offer a greater potential of structural biocompatibility than homogenous materials .

Of all the Polymer matrix composites, epoxy resins outperform most of the resins in terms of mechanical properties and resistance to environmental degradation and also biocompatibility (Ioannis, Bell And Larz).The ring structure of the epoxy helps in absorbing mechanical and thermal stresses better than the linear structure which improves the fracture toughness, stiffness and heat resistant properties. These epoxy resins have been widely used as fiber-reinforced composite matrix in industrial and aerospace fields. But in recent years, infusion of very small weight percentage of nano particle loadings into the matrix has become a common method to improve the properties of the epoxy polymer from the atomic level. Molecular forces and bonding and interactions at atomic level dictate the macroscopic properties of the materials. The nano particles have larger surface to volume ratio increasing the interactions among the atoms. Due to the high density of defects in nanocrystalline state, large fraction of atoms sits close to a defect. As a result, the materials become strong, hard with improved wear resistance and corrosion resistance so, a study of properties of polymer composites is conducted by fabricating a bone with an epoxy polymer.

Mimics was used to revert the threshold of the CT scanned images and a negative surface was created which resembled the bone marrow part inside the trabecular bone. The negative part was converted to .stl format and was imported to the 3d printing device software and was scaled up to 100 times.

Makerbot replicator 2x was used to print the negative part as a mold. Dissolvable abs plastic material was used to print the mold which can be dissolved in a powerful chemical limonene. The mold was filled with processed liquid epoxy and Silicon Carbide. These liquids take one day to be hardened and get completely solid. After making the liquids into solid the whole assembly of abs plastic and epoxy or sic was kept immersed in a container filled with concentrated limonene. Depending on the amount of dissolvable abs plastic, time varied to dissolve the complete plastic from the assembly.

7.1 Manufacturing of the Mold for Bone Structure

The mold for the bone structure is fabricated by a 3D printing. It is an addictive manufacturing technique that produces a three dimensional object from a 3D digital model by successive layering of extruded molten polymer which immediately hardens. A dissolvable filament called High Impact Polystyrene Filament (HIPS) - 1.75 mm which dissolves in limonene is used to print the mold of the bone.

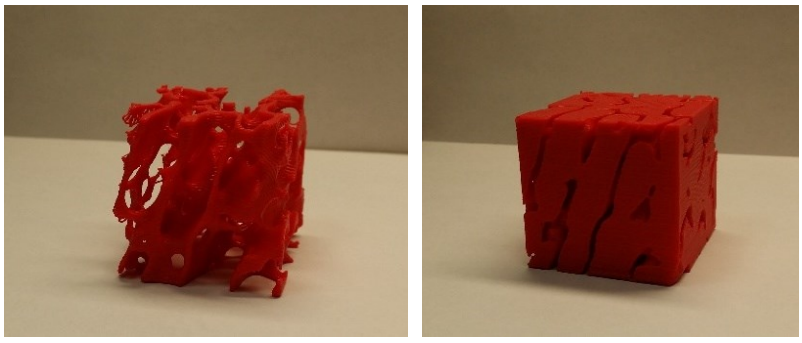

Figure 7-1 (a) 3D printed trabecular bone (b) 3D printed reverse part of trabecular bone

7.2 Preparations for Epoxy Polymer

SC-15 epoxy resin is used to make the bone structure.SC-15 is a two phased toughened epoxy resin system which cures at room temperature. It contains two parts - Part A (mixture of: Diglycidylether of Bisphenol A, 60–70%, Aliphatic Diglycidylether,10–20% and epoxy toughener 10–20%)and Part B (hardener, cycloaliphatic amine 70–90% and polyoxylalkylamine 10–30%. Part A and Part B are mixed in 10:3 ratio by weight and mechanically stirred for about 10 minutes (Chisholm and Mahfuz).

7.3 Preparation of Nanophased Epoxy Polymer

The nano particles that are used as fillers in the epoxy matrix are of Silicon carbide. They are SiC - β particles (97 % purity) of spherical shape with a diameter of 10 nm. The SiC filled epoxy composite is prepared in two steps. Firstly, part A of SC-15 is premixed with SiC particles and the mixture is placed in an ultrasonic liquid processor at 20 KHz for about 30 min. In this process, high energy acoustic waves creates numerous transient cavities around the ultrasonic probe which in turns produces an impulsive shock that breaks up the clusters and disperses the particles uniformly in the resin.[9-11].Then finally hardener (part B) is added to the resulting mixture in 10:3 ratio and slowly stirred for 10 min.

7.4 Procedure

Finally both the pure epoxy mixture and nano SiC phased epoxy mixture are seeped through separate molds from the open side of the sealed mold until it is completely filled with resin. Then the top surface is wiped flat to remove any excess epoxy resin. Then the resin is allowed to cure for 20-24 hrs. After 24 hours, the epoxy resin hardens and forms a strong solid epoxy polymer.

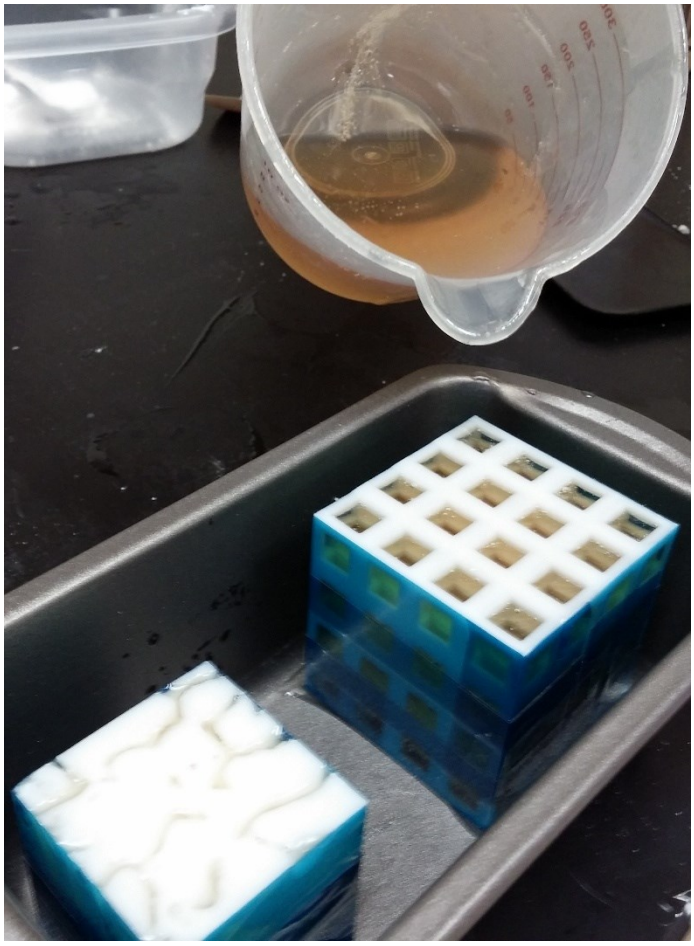

Figure 7-2 Pouring liquid epoxy in a reverse trabecular mold and in a rectangular prism assembly

Then the seal wrapped around the mold is removed and the sample is immersed in limonene until HIPS completely dissolves and the actual bone structure remains. It may take 2-3 days to completely dissolve the material depending upon the size of the sample. Rigorous stirring frequently can expedite the dissolving process. Thus two bone structures one with pure epoxy polymer and the other with nano SiC phased epoxy polymer are obtained.

7.5 Compression Test

The manufactured trabecular bone shaped models made form pure epoxy polymer and nano SiC phased epoxy polymer was subjected to compression test. From the compression tests it was observed that for both the materials the bottom part starts crushing. The top part from where compression was applied doesn't deform. At 5% strain the pure epoxy model started to shear and the nano SiC phased epoxy polymer started to shear at 10% strain.

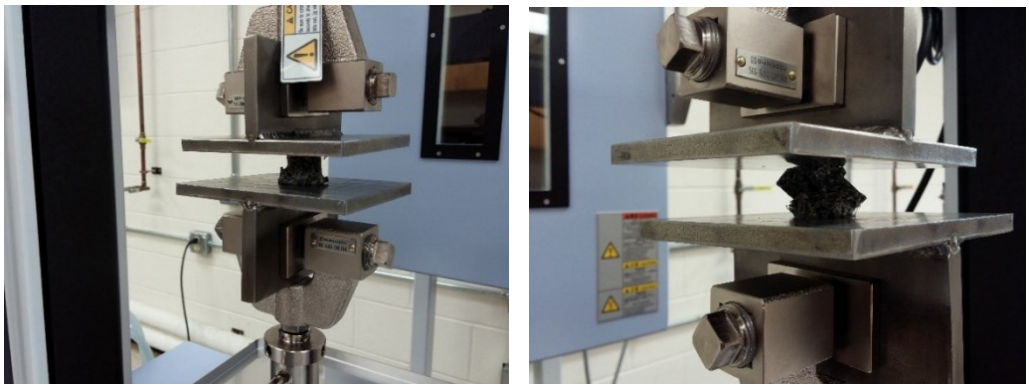

Figure 7-3 (a) Crushing of the bottom part of an epoxy trabecular bone (b) Shear of an epoxy trabecular bone

7.6 Experimental Compression Test Results

From the experimental test results the following stress-strain curve was obtained. Till the first drop in stress both the models were showing vertical crush at the bottom part. Then both of them started showing shear.

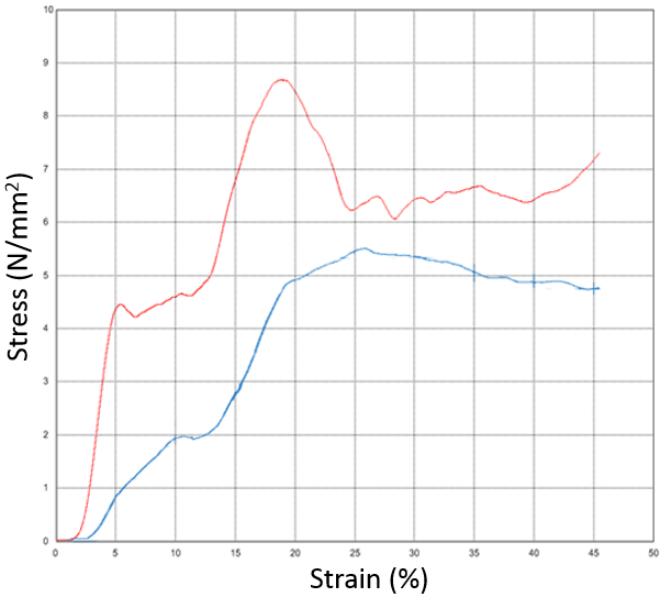

Figure 7-4 Stress-strain curve of nano phased epoxy polymer (red) and epoxy polymer (blue) obtained from experimental compression test

Chapter 8

Conclusion

Bone fracture is one of the most common health risks that increases gradually with age. The more severe the osteoporosis is the more structural degradation in bones occurs, which eventually make bones more fracture prone. The mechanical behavior of bone depends on the structural response of bone constituents over a broad range of length scales spanning from the nanoscale collagen fibril level to the macroscale trabeculae level. In this study the mechanical properties were bone were studied from composite point of view in different scales. A bottom up elastic properties set was developed to estimate the fracture toughness and elastic modulus of structures with void. Three dimensional approximated microstructures were developed to represent the heterogeneous trabecular bone geometry. CT scan based real bones were used to compare the results.

8.1 Summary

- A multiscale constitutive model to estimate the mechanical properties of bone was developed from the basic building blocks of bone. The mathematical model delivers an overall elastic constant for each scale from nano to macro. The variation of the properties in each scale was observed. A transversely isotropic model was developed using composite theories. The longitudinal elastic modulus was found to be 6.37 GPa and the transverse elastic modulus was found 2.07 GPa.
- The effect of density was studied in the micro scale of bone structure. Several real trabecular bones were obtained from CT scan images. Human, pig and rat bones were analyzed to observe the effect of density on fracture properties on trabecular bone. The overall results indicated that the fracture properties of denser structures are better. A relation was drawn from the results between fracture toughness and

apparent density. It was found that in general for the the value of fracture toughness of a trabecular structure is 0.04 times its apparent density when the fracture toughness is in MPa√m and the apparent density in g/cm^3.

- A comparative structural stiffness was studied to observe the change in the elastic properties with apparent density. All the elastic modulus values for the different real CT trabecular geometry found were plotted and an exponential relation between elastic modulus in MPa and apparent density in g/cm^3.

$$Elastic\ Modulus = 0.019e^{(0.18 \times Apparent\ Density)}$$

- Five different microstructures were generated from five different open cell units which were analyzed with different densities and relations between fracture toughness and elastic modulus with apparent density was obtained. These results were compared with the results of trabecular bone and rhombic dodecahedron was the microstructure which has the fracture properties and elastic properties similar to the real trabecular bone microstructure. The results were compared and the accuracy percentage was more that 80% for the fracture properties and the elastic properties were more than 85% similar with the trabecular bone.

8.2 Future Scope

- In this study the presence of bone marrow was not observed, hence the bone marrow interaction can be included instead of the void parts in simulating the geometries. In that case the results from both the real CT scan images and the artificial microstructures will be compared to wet bone experimental results.
- The composite theory Halpin Tsai was used to predict the combine properties of the bone in nanoscale from Collagen and Hydroxyapatite. This study can be improved by using and comparing other composite theories. An advanced

multiscale constitutive law can be developed calculate the combined properties and elastic constants for every scale more convincingly.

- In this study a modified virtual crack closure method was used to predict the fracture properties of the microstructures. This model is purely appropriate for brittle materials. Bone is a changing material that shows both brittle and ductile properties. An appropriate method can be developed to estimate the fracture properties accurately.
- Elastic properties were calculated in this study as a function of apparent density. A method of improving the elastic properties and fracture toughness can be developed.
- Five different comprehensive artificial microstructures from different open cell units were developed to compare the properties with real trabecular bone. A more convenient purely lossless space packing open cell unit can be developed to represent trabecular accurately.
- An element for finite element analysis can be developed from one the selected microstructures which matches the trabecular bone most. The element would works in such a way that it would be able to convert a solid block to the closest possible geometry of trabecular bone by inserting voids and open spaces and struts.
- Three dimensional printing is a new and promising technology, this technology can be used to print the bone microstructures with different materials and conduct tensile, compression and bending test.

The final conclusion of the study indicates that assemblies created from rhombic dodecahedron unit cell shows properties that are close to real CT scan trabecular structures. Instead

of using real trabecular structures for fracture test and other tests, rhombic dodecahedron unit cell can be modified and assemblies from this cell can be used.

Appendix A

Nomenclature

E_f	Elastic modulus of fiber
E_m	Elastic modulus of matrix
L	Length
W	Width
H	Height
A	Area
L_f	Length of fiber
D_f	Equivalent of diameter of fiber
G_f	Shear modulus of fiber
G_m	Shear modulus of matrix
V_f	Volume fraction of fiber
V_m	Volume fraction of matrix
ν_f	Poisson's ratio of fiber
ν_m	Poisson's ratio of matrix
η_L	Constant
η_T	Constant
η_G	Constant
E_{11}	Elastic modulus in longitudinal direction
E_{22}	Elastic modulus in radial direction
E_{33}	Elastic modulus in radial direction
G_{12}	Shear modulus in longitudinal direction
G_{23}	Shear modulus in radial direction
G_{23}	Shear modulus in radial direction
ν_{12}	Poisson's ratio in longitudinal direction
ν_{23}	Poisson's ratio in radial direction

ν_{13}	Poisson's ratio in radial direction
$E_{11\text{-}i}$	Longitudinal Elastic modulus in i scale
$E_{22\text{-}i}$	Radial Elastic modulus in i scale
$G_{12\text{-}i}$	Shear modulus in i scale
$\nu_{12\text{-}i}$	Poisson's ratio in i scale
$V_{f\text{-}i}$	Volume fraction of fiber in i scale
$V_{m\text{-}i}$	Volume fraction of matrix in i scale
$E_{w\text{-}i}$	Elastic modulus of water in i scale
$V_{w\text{-}i}$	Volume fraction of water in i scale
$C_{11\text{-}f}$	Compliance constant of fiber
$C_{12\text{-}f}$	Compliance constant of fiber
$C_{11\text{-}m}$	Compliance constant of matrix
$C_{12\text{-}m}$	Compliance constant of matrix
Kf	Plane strain bulk modulus of fiber
Gm	Shear modulus of matrix
Km	Plane strain bulk modulus of matrix
G23f	Shear modulus of fiber in 2-3 direction
K2	Transverse plane strain bulk modulus
ν23	Poisson's ratio in 2-3 direction
bij	Reduced elastic compliances
Cij	Elastic constants
u	Applied displacement
F	Force measured
a	Length of strut
σ_{tip}	Maximum stress at crack tip

σ_{ult}	Ultimate stress of average bone
G_I	Energy release rate
K_I	Stress intensity factor
K_{IC}	Critical stress intensity factor

References

Adnan, A., C.T.Sun, 2010. Evolution of nanoscale defects to planar cracks in a brittle solid. Journal of the Mechanic sand Physics of Solids 58, 983-1000.

Ashman, R.B., Cowin S.C., Van Buskirk W.C., Rice J.C., 1984. A continuous wave technique for the measurement of the elastic properties of cortical bone. Journal of Biomech 17(5), 349–361.

Bartl, R., Frisch B., 2009. Osteoporosis: Diagnosis, Prevention and Therapy. 2nd Revised Edition, Springer-Verlag, Berlin, Heidelberg.

Bayraktar, H.H., Morgan, E.F., Niebur G.L., Morris G.E., Wong E.K., Keaveny T.M., 2004. Comparison of the elastic and yield properties of human femoral trabecular and cortical bone tissue. Journal of Biomech 37, 27– 35.

Buehler, M.J., 2006. Nature designs tough collagen: Explaining the nanostructure of collagen fibrils. PNAS 103(33), 12285–12290.

Cooper, C., Woolf, A., 2007. Osteoporosis: Best Practice and Research Compendium. Clinical Rheumatology 26(11), 770-3198.

Currey, J.D., 2002. Bones. Princeton University Press.

Currey J.D., 1979. Mechanical properties of bone tissues with greatly different functions. Journal of Biomech 12, 313-319.

Choi, S. and Sankar, V., 2003. Fracture Toughness of Carbon Foam. Composite Materials 37(23), 2101-2116.

Cook, R.B., Zioupos, P., 2010. The fracture toughness of cancellous bone. Journal of Biomechanics 43(7), 1441.

Evans F.G., 1973. Mechanical Properties of Bone. Thomas, Springfield.

E. Specht, The best known packing of equal circles in a circle. <http://www.packomania.com/>.

Fratzl, P., Misof, K., Zizak, I., 1997. Fibrillar Structure and Mechanical Properties of Collagen. Journal Of Structural Biology 122, 119–122.

Gibson, L.J., Ashby, F., 1999. Cellular Solids: Structure and Properties. Cambridge University Press.

Glen L Niebur, Michael J Feldstein, Jonathan C Yuen, Tony J Chen, Tony M Keaveny, 2000. Highresolution finite element models with tissue strength asymmetry accurately predict failure of trabecular bone. Journal of biomechanics 33(12), 1575-1583).

Halpin, J.C., Kardos, J. L., 1976. The Halpin-Tsai Equations: A Review. Polymer Engineering And Science 16(5), 344-352.

Hamed, E., Jasiuk, I., Yoo, A., Lee, Y., Liszka,T., 2012. Multi-scale modelling of elastic moduli of trabecular bone. J. R. Soc. Interface 9, 1654-1673.

Hull D., Clyne T.W., 1996. An Introduction to Composite Materials, Cambridge University Press.

Isaac M. Daniel, Ori Ishai, 1994. Engineering Mechanics of Composite Materials, Oxford University Press.

Ilic, S., Hackl K., Gilbert R., 2010. Application of the multiscale FEM to the modeling of cancellous bone. Biomech Model Mechanobiol 9, 87–102.

Jager, I. and Fratzl, P., 2000. Mineralized Collagen Fibrils: A Mechanical Model with a Staggered Arrangement of Mineral Particles. Biophysical Journal 79, 1737–1746.

Mccullough, K.Y.G., Fleck, N.A., Ashby, M.F., 1999. Toughness Of Aluminium Alloy Foams. Pergamon Acta mater 47, 2331-2343.

Norman, T.L., Vashishth, D., Burr, D.B., 1995. Fracture toughness of human bone under tension. Journal of Biomechanics 28(3), 309-320.

Porter, D., 2004. Pragmatic multiscale modelling of bone as a natural hybrid nanocomposite. Materials Science and Engineering 365, 38–45.

Prockop, D.J., Fertala A., 1998. The Collagen Fibril: The Almost Crystalline Structure. Journal of Structural Biology 122: p. 111–118.

Rho, J.Y., L.K. Spearing, and Zioupos P., 1998. Mechanical properties and the hierarchical structure of bone. Medical Engineering & Physics 20, 92–102.

Reilly, D.T., Burstein .H., Frankel V.H., 1974. The elastic modulus of bone. Journal of Biomechanics 7, 271–275.

Rubin, M.A., Jasiuk I., 2005. The TEM characterization of the lamellar structure of osteoporotic human trabecular bone. Micron 36, 653–664.

Sih, G.C., Paris, P.C., Irwin, G.R., 1965. On cracks in rectilinearly anisotropic bodies. International Journal of Fracture 1, 189–203.

Thiyagasundaram P., Wang J., Sankar B.V., Arakere N.K. 2011. Fracture toughness of foams with tetrakaidecahedral unit cells using finite element based micromechanics. Engineering Fracture Mechanics 78, 1277–1288.

Wang, J., 2007. Fracture Toughness Of Cellular Materials Using Finite Element Based Micromechanics. Dissertation, Doctor of Philosophy, University of Florida.

Zysset P.K., Guo X.E., Hoffler C.E, Moore K.E., Goldstein S.A., 1999. Elastic modulus and hardness of cortical and trabecular bone lamellae measured by nanoindentation in the human femur. Journal of Biomechanics 32, 1005–1012.

S.Ramakrishna,J.Mayer,E Wintermantel,Kam W Leong, "Biomedical applications of polymer-composite materials" DOI: 10.1016/S0266-3538(00)00241-4

Ioannis N. Hadjinikolaou, James P. Bell And Larz Spangberg (1987). Fast Curing Epoxy And Episulfide Resins For Biomedical Applications. MRS Proceedings, 110, 451 doi:10.1557/PROC-110-451.

J. Jancar, J. F. Douglas, F. W. Starr, S. K. Kumar, P. Cassagnau, A. J. Lesser, S. S. Sternstein, and M. J. Buehler. "Current issues in research on structure-property relationships in polymer nanocomposites" Polymer 51 (2010): 3321-3343.

J.T.Han,K.Cho "Nanoparticle-induced enhancement in fracture toughness of highly loaded epoxy composites over a wide temperature range ,J Mater sci 41 (2006) 4239–4245

William Gacitua E. 1 – Aldo Ballerini A.2 – Jinwen Zhang, "Polymer nanocomposites: synthetic and natural fillers" Ciencia y tecnología 7(3): 159-178, 2005.

Kalfus J, Jancar J. Journal of Polymer Science, Polymer Physics Edition 2007;45:1380.

Freedman, David H. "Layer By Layer." Technology Review 115.1 (2012): 50–53.Academic Search Premier. Web. 26 July 2013.

Nathaniel Chisholm, Hassan Mahfuz *, Vijaya K. Rangari, Adnan Ashfaq, Shaik Jeelani, "Fabrication and mechanical characterization of carbon/SiC-epoxy Nanocomposites" Composite Structures 67 (2005) 115–124.

Eskin GI. Broad prospects for commercial application of the ultrasonoic (cavitation) melt treatment of light alloys. Ultrason Sonochem 2001:319.

Price GJ. Ultrason Sonochem 2003;10:277.

Amal Nassar, Eman Nassar*, "Study on Mechanical Properties of Epoxy Polymer Reinforced with NanoSiC particles ." Nanoscience and Nanoengineering 1(2): 89-93, 2013

Biographical Information

Md Farzad Sarker was born and raised in Dhaka, Bangladesh. He received Bachelor's degree in Mechanical Engineering from Islamic University of Technology, Dhaka, Bangladesh in November 2008. He moved to Arlington, Texas for higher education in Fall 2009. He finished Master of Science in Mechanical Engineering in May 2011. He then started Ph.D. from August 2011 in Mechanical Engineering under the supervision of Dr. Ashfaq Adnan. His research was focused on multiscale analysis of hierarchical structures and degradation mechanics of bone and bone like materials.